Synoptic Development in a Two-and-One-Half-Layer Contour Dynamics System

R. R. TRIELING AND W. T. M. VERKLEY

Royal Netherlands Meteorological Institute, De Bilt, Netherlands

(Manuscript received 21 August 2001, in final form 5 September 2002)

ABSTRACT

Synoptic development is studied using a two-and-one-half-layer contour dynamics model in full spherical geometry. The model has three isentropic layers: two lower layers that are dynamically active and one upper layer that is kept motionless. The isentropic layers cover the whole sphere and are confined in the vertical direction by two rigid horizontal boundaries. The model is assumed to be in hydrostatic and geostrophic equilibrium; forcing/friction and diabatic heating/cooling are neglected. In both active layers, the horizontal structure is represented by a piecewise-uniform distribution of potential vorticity with a single front in each layer. The potential vorticity front in the upper active layer can be associated with the tropopause or, to be more specific, with the sudden change in height of the tropopause at the jet stream. The potential vorticity front in the lower active layer enhances the baroclinicity of the system and may be associated with the polar front. Because of the assumption of hydrostatic and geostrophic equilibrium, the model atmosphere is completely defined by the instantaneous positions of the contours and can be integrated in time using the technique of contour dynamics. It is shown that realistic zonal flows can be obtained by a suitable choice of parameters. A linear stability analysis reveals that small-amplitude perturbations of given planetary wavenumber may grow for only specific latitudinal positions of the potential vorticity fronts. The maximum growth rates and highest planetary wavenumbers are found for potential vorticity fronts that are located at approximately the same latitude. Because of the conceptual simplicity of the model, in which the potential vorticity structure is represented by only two contours, the instability mechanism expresses itself in a clear way. The contour dynamics model also captures the nonlinear stages of cyclogenesis remarkably well, as is evident from the time evolution of the fronts and the time evolution of a passive tracer in a numerical simulation of a cutoff cyclone.

1. Introduction

The origin and development of midlatitude cyclones continues to be an important subject of research in dynamic meteorology. There are at least two reasons for this: individual cyclones are, to a large extent, responsible for the variation in daily weather, whereas their collective transport properties shape the mean atmospheric circulation. Early attempts by Bjerknes (1919) and Bjerknes and Solberg (1921, 1922) to explain the life cycle of midlatitude cyclones using the concept of a polar front were of great value but remained in essence qualitative. The modern quantitive approach has its origin in the studies by Charney (1947) and Eady (1949), who showed that smooth baroclinic zonal flows of realistic magnitude can become unstable and develop structures resembling midlatitude cyclones both in spatial scale and rate of development. Shortly after the publication of these studies, two papers by Phillips (1951, 1954) appeared in which the smooth vertical profiles used by Charney and Eady were represented in terms of two discrete layers or levels. The analysis became considerably simpler while the essence of the original conclusions was maintained. Bretherton (1966a,b) continued this line of approach by using the concept of potential vorticity to clarify the mechanism of baroclinic instability. In the second of the two cited papers, Bretherton showed how the surface potential temperature variations, which are the only dynamically active components in Eady's model, can be reconciled with Phillips's two-layer representation.

The current paper builds further on the approach by Phillips (1951, 1954) and Bretherton (1966a,b) by extending Phillips's use of a vertical discretization in terms of layers and Bretherton's analysis in terms of potential vorticity. Our aim is to clarify the mechanism of baroclinic instability and synoptic development in a setting that is simple and realistic at the same time. We use a layered vertical representation of the flow because, as noted by Pedlosky (1987), a vertical discretization in terms of a finite number of material layers has the advantage that it leads to an idealized but physically realizable system. In the current study, layers of constant density are replaced by layers of constant specific entropy (potential temperature) to render the system more

Corresponding author address: Dr. Ruben R. Trieling, Fluid Dynamics Laboratory, Department of Applied Physics, Eindhoven University of Technology, P.O. Box 513, 5600 MB Eindhoven, Netherlands.
E-mail: r.r.trieling@tue.nl

relevant as a model of the atmosphere. We also add a passive stratospheric layer to the original two-layer system [a suggestion already made by Phillips (1951)] to obtain a two-and-one-half-layer system, and we work in full spherical geometry. We describe the flow in the two active layers in terms of piecewise-uniform distributions of potential vorticity, with a single discontinuity (front) in each active layer. Assuming that the system is in hydrostatic and geostrophic balance (actually a simplified form of linear balance), and ignoring mechanical forcing/friction and diabatic heating/cooling, this implies that the whole system can be described in terms of the positions of the two fronts.

For the upper active layer, the assumption of a single front in potential vorticity is a realistic description of the flow at isentropic surfaces higher in the atmosphere. Indeed, on these isentropes the potential vorticity field is often characterized by a steep gradient at the tropopause [a recent reference is Haynes et al. (2001)]. For the lower active layer, this assumption is less well founded, but it is a way of modeling surface potential temperature variations. As Bretherton (1966b) pointed out, the potential vorticity distribution in the bottom layer of Phillips's (1951) model may be interpreted as a vertically distributed representation of the surface potential vorticity sheet associated with the true surface potential temperature variations in Eady's (1949) model. The upper potential vorticity front causes a sharply peaked velocity field and steep gradients in the thickness of the upper active layer. The upper potential vorticity front may therefore be associated with the tropopause or, to be more specific, with the sudden change in tropopause height at the jet stream, the so-called tropopause break (Palmén and Newton 1969). The lower front in potential vorticity enhances the downward bowing of the bottom layer's upper interface and thereby increases the baroclinicity of the flow. When looked upon from the perspective of a height or pressure surface at a sufficiently large distance from the surface, the downward bowing of this interface manifests itself as a discontinuity in potential temperature. It is for this reason that we associate the lower potential vorticity front with the polar front. It should be kept in mind, however, that at the surface of our model there are no real potential temperature contrasts because the bottom layer of the model covers the whole sphere.

Because the incorporation of geostrophic equilibrium in a layered isentropic model in full spherical geometry is not standard we describe our model in some detail in section 2, referring to the appendix for matters of technique. We then discuss in section 3 the properties of the basic zonal flows that can be constructed with two fronts of potential vorticity in the active layers. The flows are characterized by a sharp jet in the upper active layer and, depending on the choice of the system parameters, a sharp jet in the lower active layer. We also study how the interface heights of the different layers vary in the neighborhood of the potential vorticity fronts because it will clarify how the two fronts in potential vorticity can be related to the tropopause and the polar front. The study of zonal flows produced by potential vorticity discontinuities has revealed the necessity of moderate values of the Rossby radii of both the equivalent barotropic and baroclinic vertical mode of the system. These values could only be achieved by adding a passive stratospheric layer to the original two-layer system. The necessity of a moderate value of the Rossby radius of deformation is in accord with an earlier study by Verkley (1994), who used the equivalent barotropic vorticity equation instead of the barotropic vorticity equation in order to reconcile a single front in potential vorticity with realistic values of the velocity.

The two following sections of the paper contain our main results. Section 4 contains an analytic treatment of the linear stability of the zonal flows described in the previous section. In the spirit of Bretherton (1966a,b) it will be demonstrated that the potential vorticity view gives a clear insight into the essence of baroclinic instability because it reveals how a phase shift between the waves in the upper and lower contours induces a positive feedback that leads to growth. It will also be shown that the growth rate depends on the latitudinal positions of the potential vorticity fronts and that the maximum growth rates are found if the potential vorticity fronts are located at approximately the same latitude. Section 5 addresses the evolution of nonlinear waves using the numerical contour dynamics technique and demonstrates that the model atmosphere is capable of producing realistic synoptic developments. As an example, we show the development of a cutoff cyclone. A comparison is made with the evolution of a cutoff cyclone as forecast by the global weather prediction model employed at the European Centre for Medium-Range Weather Forecasts (ECMWF). The main results are summarized and the conclusions are given in section 6.

2. The model

The two-and-one-half-layer model has three isentropic layers, which are assumed to cover the whole sphere: an upper layer with potential temperature θ^0, a layer beneath it with potential temperature θ^1, and a surface layer with potential temperature θ^2, where $\theta^0 > \theta^1 > \theta^2$ (see Fig. 1a). The flow is confined in the vertical by two rigid horizontal boundaries at $z = z_0$ and $z = z_3$. The height of the lower system boundary z_3 corresponds to the level of the spherical surface and is set to zero, whereas the height of the upper system boundary z_0 is determined by the rest-state mass distribution and the requirement that the pressure at $z = z_0$ is zero. The upper boundary condition implies that the top layer is motionless. Since the model has spherical geometry, positions and velocities are defined in a spherical coordinate system (λ, ϕ, z) that is fixed to the earth, where λ is longitude, ϕ is latitude, and z is the vertical distance above mean sea level. The earth is assumed to be a

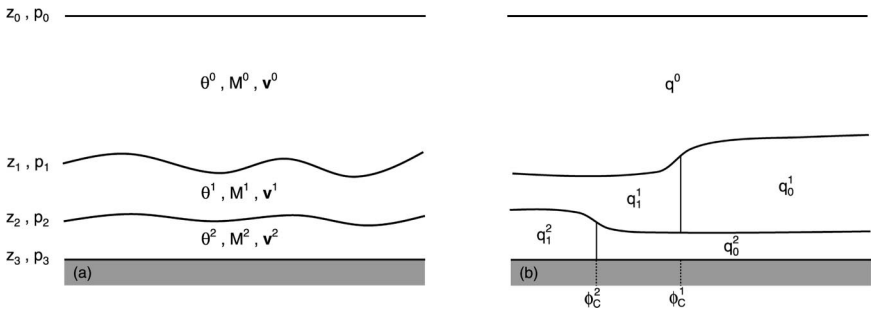

FIG. 1. (a) Schematic cross section of the two-and-one-half-layer model that has three layers with constant potential temperatures θ^0 (upper layer), θ^1 (middle layer), and θ^2 (lower layer). The flow is confined in the vertical by two rigid horizontal boundaries at $z = z_0$ and $z = z_3$, with corresponding pressures $p_0 = 0$ and p_3, respectively. Within each layer both the Montgomery potential M^i and the horizontal velocity $\mathbf{v}^i$ are independent of height but discontinuous at the interfaces z_1 and z_2 where the pressures are p_1 and p_2, respectively. (b) Schematic cross section of the two-and-one-half-layer model for a zonal flow produced by a potential vorticity front $\Delta q^1 = q_1^1 - q_0^1$ at latitude ϕ_C^1 in layer 1 and a potential vorticity front $\Delta q^2 = q_1^2 - q_0^2$ at latitude ϕ_C^2 in layer 2.

perfect sphere with radius $a = 6.371 \times 10^6$ m, rotating at an angular velocity $\Omega = 7.292 \times 10^{-5}\ \mathrm{s}^{-1}$. Distance is expressed in units of a and time in units of Ω^{-1} so that the Coriolis parameter is given by $f = 2 \sin \phi$ and the earth's radius a in the differential operators is replaced by 1. We take the unit vectors **i**, **j**, and **k** to be directed in the eastward, northward, and upward direction, respectively, so that the horizontal velocity **v** can be written as $u\mathbf{i} + v\mathbf{j}$, with u and v being the velocity components in the eastward and northward directions.

The potential temperature θ is defined as $\theta = T(p_r/p)^\kappa$, where T is the absolute temperature, p is the pressure, and p_r is a constant reference pressure of 1000 hPa. The exponent κ is defined by R/c_p, where R is the gas constant of dry air and c_p is the specific heat of dry air at constant pressure. The absolute temperature T and pressure p are related by the ideal-gas law $p = \rho RT$, where ρ is the density. It is assumed that the model atmosphere is in hydrostatic equilibrium so that in each layer $\partial p/\partial z = -\rho g$, where g is the acceleration due to gravity. The latter assumption, in combination with the ideal-gas law and the assumption that in each layer the potential temperature is uniform, fixes the vertical structure of the absolute temperature, pressure, and density. In particular, the absolute temperature decreases linearly with height according to the dry-adiabatic lapse rate g/c_p. It follows from the foregoing that the Montgomery potential M, defined as $M = gz + c_pT$, is uniform with height in an isentropic layer, as a consequence of which it may be consistently assumed that the horizontal velocity **v** is also uniform with height.

Diabatic processes and friction are assumed to be absent so that the potential vorticity P, defined in layer i as $P^i = (f + \zeta^i)/(\eta_{i+1} - \eta_i)$, is materially conserved (see, e.g., Verkley 2000, 2001). Here, ζ^i is the relative vorticity in layer i, and η_{i+1} and η_i are the normalized pressures at the boundaries z_{i+1} and z_i, respectively, where $\eta = p/p_r$. In addition, the model atmosphere is assumed to be in a form of geostrophic equilibrium that is a simplification of ''linear balance'' (Daley 1983). This simplest form of the geostrophic relationship—as Daley called it—can be dealt with easily and does not lead to unrealistic behavior at the equator (Verkley 2001). The simplified linear balance condition relates both the horizontal velocity **v** and the Montgomery potential M in layer i to the streamfunction ψ in layer i; that is,

$$\mathbf{v}^i = \mathbf{k} \times \nabla \psi^i, \tag{1}$$

$$M^i = \overline{M}^i + f\psi^i, \tag{2}$$

where $\overline{M}^i$ is the constant rest-state value of the Montgomery potential in layer i and ∇ is the horizontal gradient operator. Note that the relative vorticity ζ^i can be written in terms of the streamfunction ψ^i by $\zeta^i = \nabla^2\psi^i$, where ∇^2 is the horizontal Laplace operator. Like the Montgomery potential M^i, the normalized pressure field η_i, evaluated at interface i, is written as the sum of its rest-state value $\overline{\eta}_i$ and a deviation η_i'—that is, $\eta_i = \overline{\eta}_i + \eta_i'$—and is linearized around the state of rest, assuming that $\eta_i'/\overline{\eta}_i \ll 1$. The absolute vorticity $f + \zeta^i$ in layer i is linearized around the planetary vorticity f, assuming that $\zeta^i/f \ll 1$. It then follows from the linearization of the potential vorticity P^i (see appendix), and the assumption that the linearized potential vorticity remains materially conserved following the balanced velocity (1), that the dynamics of the two-and-one-half-layer isentropic model is governed by

$$\frac{D^i q^i}{Dt} = 0, \tag{3}$$

for $i = 1, 2$, where D^i/Dt is the horizontal material derivative for a two-dimensional scalar field advected by $\mathbf{v}^i$ on the surface of a sphere with unit radius. The fields q^i in the active layers ($i = 1, 2$) are given by

$$q^1 = f + \nabla^2\psi^1 - F^{11}\psi^1 - F^{12}\psi^2, \tag{4a}$$

$$q^2 = f + \nabla^2\psi^2 - F^{21}\psi^1 - F^{22}\psi^2. \tag{4b}$$

Note that the fields q^i are related to the original expression of the potential vorticity P in layer i by $P^i = q^i/(\overline{\eta}_{i+1} - \overline{\eta}_i)$, which expression is approximate because of the linearization. From now on we will refer to q as the potential vorticity. For the matrix of parameters F^{ij}, we have the following expressions:

$$\begin{bmatrix} F^{11} & F^{12} \\ F^{21} & F^{22} \end{bmatrix} = \begin{bmatrix} F_u^1 + F_l^1 & -F_l^1 \\ -F_u^2 & F_u^2 + F_l^2 \end{bmatrix}, \tag{5}$$

where, if we define $\theta^3 = 0$, the parameters F_l^i and F_u^i are given by

$$F_l^i = \frac{2\Omega^2 a^2}{gD_l^i}\left(\frac{\theta^i}{\theta^i - \theta^{i+1}}\right), \tag{6a}$$

$$F_u^i = \frac{2\Omega^2 a^2}{gD_u^i}\left(\frac{\theta^i}{\theta^{i-1} - \theta^i}\right), \tag{6b}$$

with

$$D_l^i = (\overline{\eta}_{i+1} - \overline{\eta}_i)\overline{\eta}_{i+1}^{\kappa-1}\kappa H^i, \tag{7a}$$

$$D_u^i = (\overline{\eta}_{i+1} - \overline{\eta}_i)\overline{\eta}_i^{\kappa-1}\kappa H^i. \tag{7b}$$

In these expressions, $H^i = c_p\theta^i/g$ is the scale height of layer i. In principle, the expressions (6) depend on f^2, but by assuming that f^2 can be approximated by its global average this factor is replaced by 2, leading to constant parameters F^{ij} and therefore to a simplification of the inversion of (4). This approximation is supported by the behavior of linear Rossby waves subject to a global version of the equivalent barotropic vorticity equation that is identical to the expression in its traditional form except for a full f^2 dependence of the stretching term. It can be shown from the dispersion relation of linear Rossby waves that, for waves with a short meridional wavelength, the above approximation is legitimate. The parameters F^{ij} measure the relative importance of vortex-tube stretching and squeezing as compared with relative vorticity. To be more specific, F_l^i is related to pressure deviations at the lower boundary of layer i, whereas F_u^i is related to pressure deviations at the upper boundary of layer i. A standard vertical-mode decomposition of the streamfunction and potential vorticity fields in (4) reveals that the eigenvalues $\tilde{F}^1$ and $\tilde{F}^2$ of the matrix of parameters F^{ij} are related to the Rossby radii of the equivalent barotropic and the baroclinic vertical modes of the system (see appendix for details).

From the distribution of the potential vorticity in layer i, one can obtain, via the streamfunction ψ^i, the pressures at the interfaces between the layers (see appendix) as well as the velocities in the layers and—because of the uniformity of θ in layer i in combination with the ideal-gas law and hydrostatic equilibrium—the complete three-dimensional structure of the model atmosphere. For a more detailed discussion of the vertical profiles in a hydrostatic isentropic layer we refer to Verkley (2000).

In each active layer we now define two regions of constant potential vorticity that are separated by a single closed contour C^i: a region around the North Pole, denoted by R_1^i, with $q^i = q_1^i$, and another region, denoted by R_0^i, corresponding to the rest of the sphere, with $q^i = q_0^i$. The potential vorticity field q^i in layer i is therefore assumed to be of the form

$$q^i(\mathbf{r}) = q_0^i + \Delta q^i \mathcal{H}^i(\mathbf{r}), \tag{8}$$

where

$$\Delta q^i = q_1^i - q_0^i, \tag{9}$$

and $\mathcal{H}^i(\mathbf{r})$ is a kind of two-dimensional Heaviside function, defined to be 1 in region R_1^i and 0 in region R_0^i; that is,

$$\mathcal{H}^i(\mathbf{r}) = \begin{cases} 1, & \mathbf{r} \in R_1^i \\ 0, & \mathbf{r} \in R_0^i. \end{cases} \tag{10}$$

Since the potential vorticity is assumed to be piecewise uniform in each active layer, the structure of the potential vorticity field is completely characterized by the contours separating the different regions of uniform potential vorticity. It is shown in the appendix that for this distribution of potential vorticity the streamfunction ψ^i and its gradient $\nabla\psi^i$—needed for the velocity $\mathbf{v}^i$—can be expressed in terms of line integrals along the contours C^i. This implies that the contours determine the state of the system and its time evolution completely.

3. Zonal flow

For the two-and-one-half-layer model, we now investigate the flow field resulting from a potential vorticity distribution that is zonally symmetric. Each active layer has two regions of uniform potential vorticity, as shown in Fig. 1b. The two fronts, denoted by C^i, can be described by

$$\phi^i(\lambda) = \phi_C^i. \tag{11}$$

The fact that the fronts in Fig. 1b are drawn by vertical lines reflects the fact that the horizontal flow in a hydrostatic isentropic layer is independent of height. In the appendix we derive an analytical expression for the zonal streamfunction Ψ^i associated with two zonal contours. The zonal velocity U^i can be obtained from this streamfunction by using (1). From the streamfunction we can also derive the pressures at the interfaces as well as the heights of the interfaces. In this way the complete three-dimensional structure of the flow is given.

As an example, we consider the case of two potential vorticity fronts that are located at the same latitude circle; that is, $\phi_C^1 = \phi_C^2 = 60.0°$. The potential temperatures are $\theta^0 = 380$, $\theta^1 = 340$, and $\theta^2 = 300$ K, respectively, being typical values for a real atmosphere. The rest-

state mass distribution is defined by the normalized rest-state pressures $\overline{\eta}_0 = 0.0$, $\overline{\eta}_1 = 0.6$, $\overline{\eta}_2 = 0.9$, and $\overline{\eta}_3 = 1.0$. The potential vorticity jumps across the fronts are set to $\Delta q^1 = 2.5$ and $\Delta q^2 = -0.5$, respectively. Both q_0^1 and q_0^2 are set to zero since these quantities do not affect the dynamics of the model atmosphere in any way, which may be inferred from expression (A29) in the appendix. With these values for θ^i, $\overline{\eta}_i$, and Δq^i, we obtain reasonable values for the Rossby radii and the zonal velocities, and the variations of the interface pressures are generally kept within the limits of our linearization assumption. Although we are not restricted to this particular choice of parameters, we will use the same values of θ^i and $\overline{\eta}_i$ throughout the rest of this paper to facilitate comparison of the model results. The jumps in potential vorticity Δq^1 and Δq^2 will be varied within the limitations of our model.

Based on the above values for θ^i and $\overline{\eta}_i$, the eigenvalues of the matrix of parameters F^{ij} are given by $\tilde{F}^1 = 77$ and $\tilde{F}^2 = 525$. The value of $\tilde{F}^1$, corresponding to the equivalent barotropic mode of the system, is of the same order as the value imposed by Verkley (1994) to obtain realistic zonal profiles using the equivalent barotropic vorticity equation. The equivalent barotropic motion in our two-and-one-half-layer model is essentially due to the pressure deviations η_1', whereas the baroclinic motion of the two layers is due to the pressure deviations η_2', which cause vortex tubes to be stretched in one layer and to be squeezed in the other. The relatively large value of $\tilde{F}^2$ indicates that stretching effects dominate baroclinic motion. This result is mainly due to layer 2 being shallow when compared with layer 1; that is, in normalized pressure coordinates, $(\overline{\eta}_1 - \overline{\eta}_2)/(\overline{\eta}_2 - \overline{\eta}_3) = 3.0$. This result may also be deduced from a comparison between the parameters F_l^1 and F_u^2, which measure the relative importance of vortex-tube stretching in layers 1 and 2, respectively, because of the deformation of interface 2. It can be verified easily that $F_u^2/F_l^1 = 3.0$.

The zonal flow profiles resulting from the two potential vorticity fronts at $\phi = 60.0°$ are shown in Figs. 2a–c, with the potential vorticities q^i, the streamfunctions Ψ^i, and the zonal velocities U^i. Solid lines correspond to layer 1, and dashed lines correspond to layer 2. In Fig. 2a, the dotted line denotes the rest-state potential vorticity in all layers, whereas the dash–dotted line denotes the potential vorticity q^0 in the passive layer. The zonal velocity profile in layer 1 is characterized by a sharply peaked westerly jet with the maximum wind speed at the upper potential vorticity front. This region of intense wind speeds may be associated with the polar jet stream. The zonal velocity in layer 2 is also westerly but weaker in magnitude. Farther south, the zonal flow is weakly easterly because of the contribution of the planetary vorticity f, with the maximum easterly wind speeds located around the equator.

For the same case, Figs. 2d–f show the fields evaluated at the interfaces, with the relative pressure deviations $\eta_i'/\overline{\eta}_i$, the normalized pressures η_i, and the interface heights z_i. The relative pressure deviations at the interfaces are generally small, as required by the linearization of P^i. At some distance south of the potential vorticity fronts, η_2' is very small, which indicates that the motion in that region is mainly equivalent barotropic. The pressure deviations η_1' merely reflect the height deviations of interface 1, whereas the pressure deviations η_3' correspond to the vertically integrated mass fluctuations per unit area at the earth's surface. We also see, however, that in the Southern Hemisphere the magnitudes of the relative pressure deviations at interface 1 exceed the value 1, which violates the linearization assumption. A remedy in this case might be the addition of two extra fronts in the Southern Hemisphere, in much the same way as we have fronts in the Northern Hemisphere. Because of the large distance of these fronts from the fronts in the Northern Hemisphere, there will be negligible interaction between these sets of fronts so that the fronts in the Southern Hemisphere do not need to be taken into account for our calculations.

Figure 2f may be interpreted as a vertical north–south view of the atmosphere, which is remarkably similar to a real meridional cross section of the atmosphere with the characteristic upward and downward bowing of the isentropes near the tropopause. Indeed, Fig. 2f has much in common with Fig. 4.7 of Palmén and Newton (1969) in which a schematic cross section is given through the jet stream and its associated polar front and tropopause. When the regions in which the potential vorticity is q^0 and q_1^1 are associated with the stratosphere, then the tropopause makes a sudden change in height at the upper potential vorticity front. Looking at Fig. 4.7 of Palmén and Newton (1969) it makes sense to associate the upper potential vorticity front with the tropopause or, rather, with the gap in the tropopause: the tropopause break. If we focus on an isobaric level cutting through interface 2, the polar front can be seen in the form of a sudden change $\theta^1 - \theta^2$ in potential temperature separating the cold air of layer 2 from the warm air of layer 1. It should be remarked, however, that when Fig. 2f is compared with Fig. 4.7 of Palmén and Newton (1969), the tropopause to the north of the polar jet stream is too low. In the next paragraph an example will be shown in which the polar tropopause is higher.

Figure 3 shows the zonal velocities U^i and the interface heights z^i corresponding to the case described above (left panels) and two other cases in which the potential vorticity fronts are either located at different latitude circles—that is, $\phi_C^1 = 65.5°$ and $\phi_C^2 = 60.0°$ (middle panels)—or are located at the same latitudes but with different values for the potential vorticity jumps—that is, $\Delta q^1 = 2.5$ and $\Delta q^2 = -2.5$ (right panels). Figure 3b shows that the flow in layer 2 is dominated by the potential vorticity distribution in layer 1, which is apparent from the strong westerly wind field U^2 at the position of the upper potential vorticity front $\phi = \phi_C^1$ and the small kink in the velocity profile U^2 at the

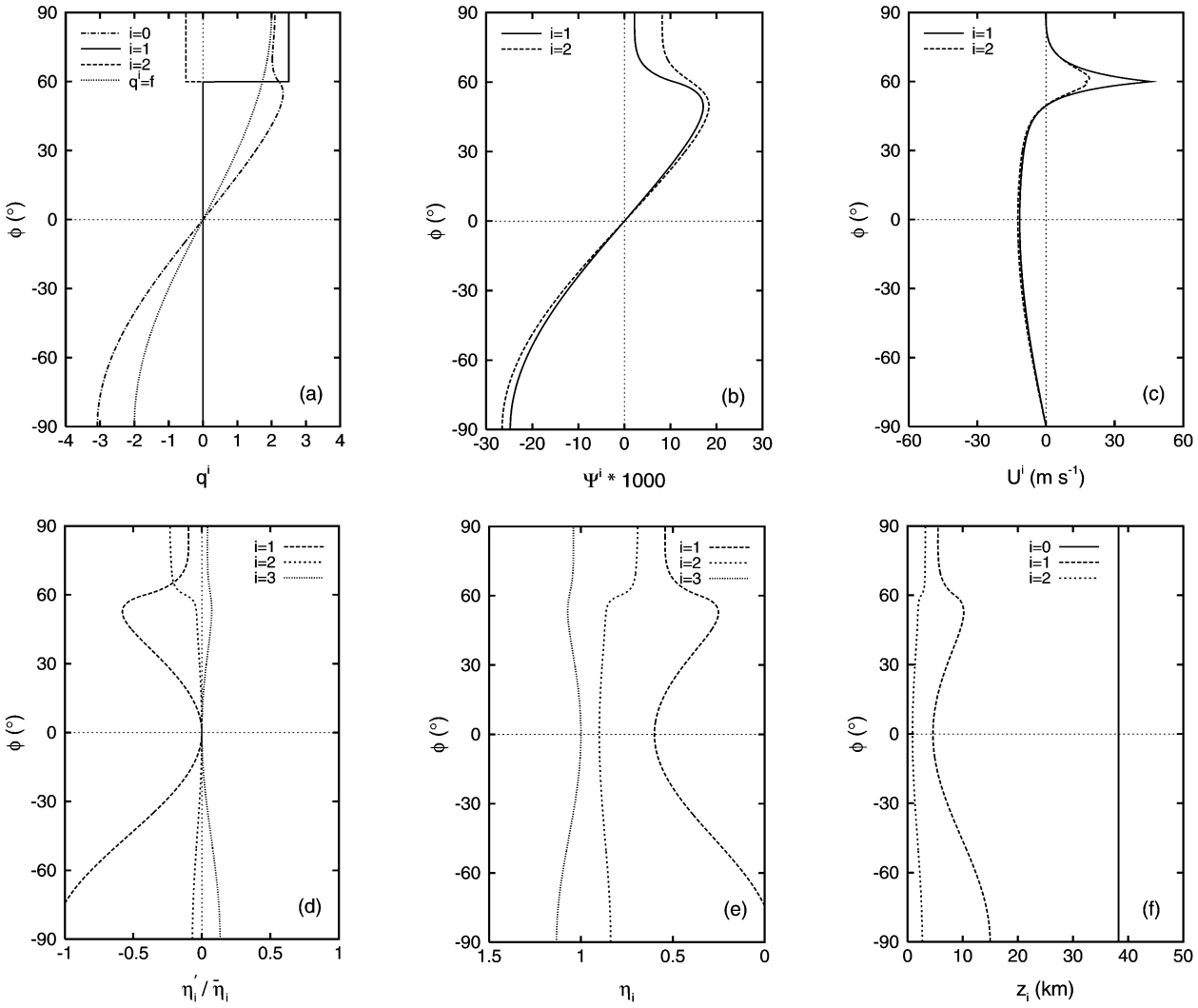

FIG. 2. (top) Zonal flow profiles resulting from two potential vorticity fronts at 60.0°N in a two-and-one-half-layer contour dynamics system with (a) the potential vorticities q^i, (b) the streamfunctions Ψ^i, and (c) the zonal velocities U^i. The dotted line in (a) corresponds to f. (bottom) Fields evaluated at the interfaces of a two-and-one-half-layer contour dynamics system with (d) the relative pressure deviations $\eta_i'/\overline{\eta}_i$, (e) the normalized pressures η_i, and (f) the heights z_i. The potential vorticity jumps are $\Delta q^1 = 2.5$ and $\Delta q^2 = -0.5$, with $q_0^1 = q_0^2 = 0.0$. The rest-state mass distribution of θ, which is used throughout this paper, is defined by $\theta^0 = 380$ K, $\theta^1 = 340$ K, $\theta^2 = 300$ K, $\overline{\eta}_0 = 0.0$, $\overline{\eta}_1 = 0.6$, $\overline{\eta}_2 = 0.9$, and $\overline{\eta}_3 = 1.0$.

position of the lower potential vorticity front $\phi = \phi_C^2$. The reason for this effect is that—owing to the different rest-state layer thicknesses—a potential vorticity jump in layer 1 is realized more as relative vorticity, whereas a potential vorticity jump in layer 2 is realized more by stretching and squeezing. Note that the zonal flow depicted in Fig. 3b is not unlike the wind profile along a frontal zone, as displayed in Fig. 8.3 of Palmén and Newton (1969). For larger magnitudes of Δq^2 (Fig. 3c), the jet at the lower potential vorticity front is more pronounced. It is also apparent that the horizontal extent of the jet in layer 1 is much broader than that in layer 2, which is again due to the different rest-state layer thicknesses. The interface heights (bottom panels) are similar in all three cases, except that in Fig. 3e the upward- and downward-bowing interfaces near the potential vorticity fronts are no longer vertically aligned because of the different positions of the potential vorticity fronts, whereas in Fig. 3f the slope of interface 2 near the lower potential vorticity front is steeper than that in Fig. 3d because of the larger value of Δq^2. Note also that in Fig. 3f the polar tropopause is now higher in the atmosphere so that the interpretation given above is closer to the truth in this case.

4. Linear stability analysis

In this section we investigate the stability of zonal flows with respect to perturbations of infinitesimal amplitude. Let us consider infinitesimal wavelike pertur-

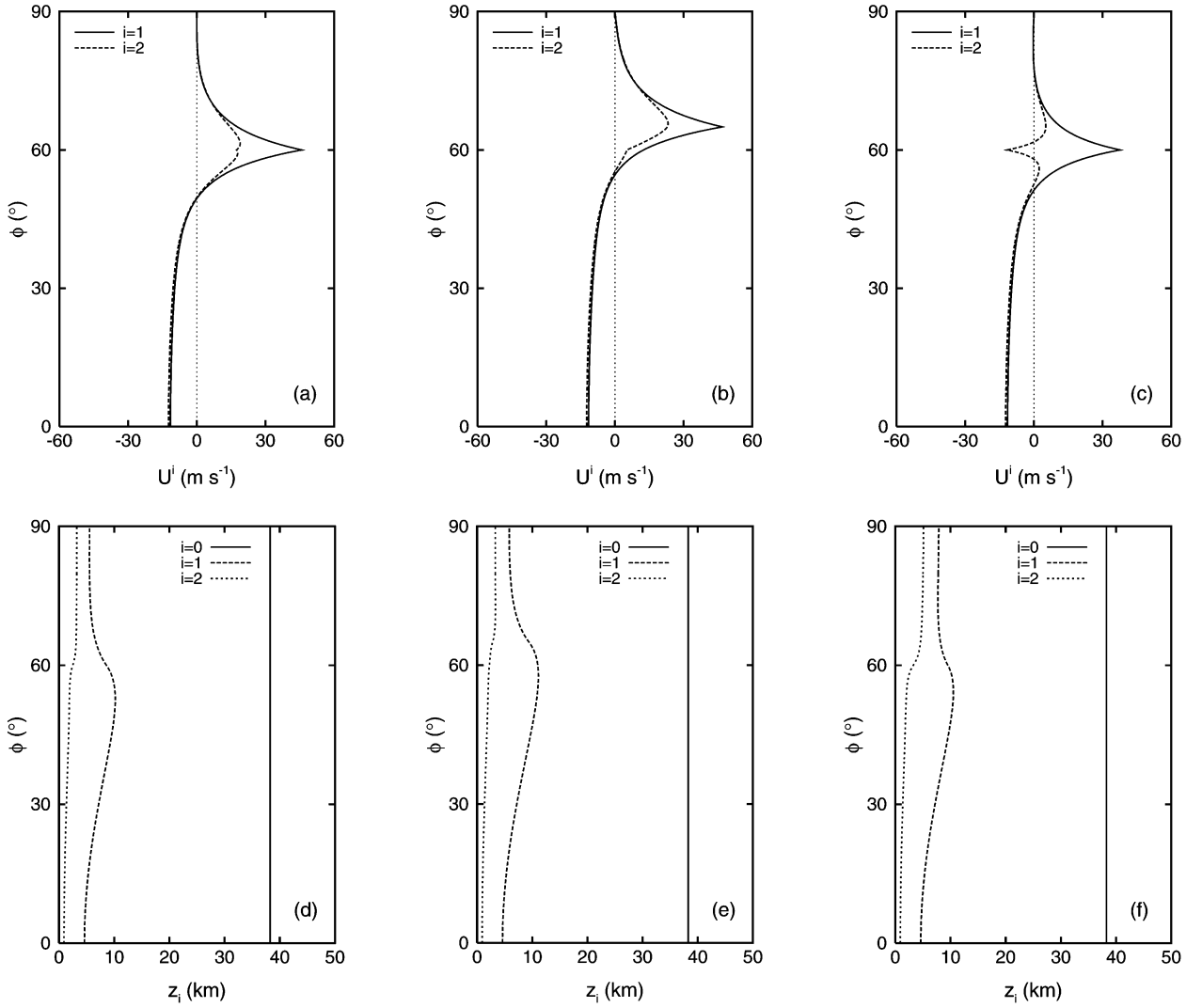

FIG. 3. (top) Zonal velocity profiles and (bottom) corresponding interface heights associated with (a), (d) $\Delta q^1 = 2.5$, $\Delta q^2 = -0.5$, and $\phi_C^1 = \phi_C^2 = 60.0°$; (b), (e) $\Delta q^1 = 2.5$, $\Delta q^2 = -0.5$, $\phi_C^1 = 65.5°$, and $\phi_C^2 = 60.0°$; and (c), (f) $\Delta q^1 = 2.5$, $\Delta q^2 = -2.5$, and $\phi_C^1 = \phi_C^2 = 60.0°$. In all cases, $q_0^1 = q_0^2 = 0.0$. The zonal wind field in (b) corresponds to the basic zonal wind field of the baroclinic wave system shown in Fig. 4.

bations of the basic-state zonal contours so that these contours are described by

$$\phi^i(\lambda, t) = \phi_C^i + \delta\phi_C^i(\lambda, t), \tag{12}$$

with

$$\delta\phi_C^i(\lambda, t) = \mathrm{Re}[\epsilon^i \exp im(\lambda - \omega t)], \tag{13}$$

where Re denotes the real part of the expression between brackets, and m is the planetary wavenumber, that is, the number of waves around a latitude circle. Both the amplitude ϵ^i and the angular phase velocity ω of the wave propagating along the basic zonal flow may be complex. It is shown in the appendix that the perturbation streamfunction can be written as

$$\delta\psi^i(\lambda, \phi, t) = \sum_j Z^{ij}(\phi)\mathrm{Re}[\epsilon^j \exp im(\lambda - \omega t)], \tag{14}$$

where the fields $Z^{ij}(\phi)$ are the contributions of the perturbation in contour j to the streamfunction in layer i. Analytical expressions for the fields $Z^{ij}(\phi)$ can be derived from the condition that both ψ^j and $\nabla\psi^j$ are continuous at the contours (see appendix). The angular velocity ω follows from the linearized kinematic condition that each point of the contour is advected by the velocity at that point; that is,

$$\frac{\partial}{\partial t}\delta\phi_C^i(\lambda, t) + \frac{U^i(\phi_C^i)}{\cos\phi_C^i}\frac{\partial}{\partial\lambda}\delta\phi_C^i(\lambda, t) = \frac{1}{\cos\phi_C^i}\frac{\partial}{\partial\lambda}\delta\psi^i(\lambda, \phi_C^i, t), \tag{15}$$

where $U^i(\phi)$ is the basic zonal velocity field. Substi-

tution of expressions (13) and (14) into (15) then leads to the following linear system in terms of ϵ^1 and ϵ^2:

$$\epsilon^1[\omega\cos\phi_C^1 - U^1(\phi_C^1) + Z^{11}(\phi_C^1)] + \epsilon^2 Z^{12}(\phi_C^1) = 0, \tag{16a}$$

$$\epsilon^1 Z^{21}(\phi_C^2) + \epsilon^2[\omega\cos\phi_C^2 - U^2(\phi_C^2) + Z^{22}(\phi_C^2)] = 0. \tag{16b}$$

Since the set of equations in (16) is homogeneous, nontrivial solutions for ϵ^1 and ϵ^2 will exist only if the corresponding determinant is zero. This condition yields the following relation for the angular velocity ω:

$$\omega = \frac{1}{2}\left[\frac{U^1(\phi_C^1) - Z^{11}(\phi_C^1)}{\cos\phi_C^1} + \frac{U^2(\phi_C^2) - Z^{22}(\phi_C^2)}{\cos\phi_C^2}\right] \pm \Delta^{1/2}, \tag{17}$$

with

$$\Delta = \left\{\frac{1}{2}\left[\frac{U^1(\phi_C^1) - Z^{11}(\phi_C^1)}{\cos\phi_C^1} - \frac{U^2(\phi_C^2) - Z^{22}(\phi_C^2)}{\cos\phi_C^2}\right]\right\}^2 + \frac{Z^{12}(\phi_C^1)Z^{21}(\phi_C^2)}{\cos\phi_C^1\cos\phi_C^2}. \tag{18}$$

If ϵ^j is written as $\epsilon^j = |\epsilon^j|\exp[i\arg(\epsilon^j)]$ and ω in terms of its real and imaginary parts—that is, $\omega = \omega_R + i\omega_I$—it follows from (13) that, for nonzero values of ω_I, the waves will grow ($\omega_I > 0$) or decay ($\omega_I < 0$) with a rate $m\omega_I$. It follows from (16a) that the ratio between the wave amplitudes is given by

$$\frac{\epsilon^2}{\epsilon^1} = -\frac{\omega_R\cos\phi_C^1 - U^1(\phi_C^1) + Z^{11}(\phi_C^1)}{Z^{12}(\phi_C^1)} - i\frac{\omega_I\cos\phi_C^1}{Z^{12}(\phi_C^1)}. \tag{19}$$

We see that for neutral waves ($\omega_I = 0$), the wave in the upper layer is either in phase or one-half of a wavelength out of phase with the wave in the lower layer, depending on the sign of the real part of (19). For unstable waves, the phase shift between the upper and lower waves lies between zero and one-half of a wavelength. Treating the case of growing/decaying waves and neutral waves separately, it can be shown by combining (17) and (18) with (19), that we have the following relation between the amplitude ratios corresponding to the two different roots of ω:

$$\left(\frac{\epsilon^2}{\epsilon^1}\right)_+\left(\frac{\epsilon^2}{\epsilon^1}\right)_- = -\frac{Z^{21}(\phi_C^2)\cos\phi_C^1}{Z^{12}(\phi_C^1)\cos\phi_C^2}, \tag{20}$$

where the different ratios are denoted by $(\epsilon^2/\epsilon^1)_+$ and $(\epsilon^2/\epsilon^1)_-$, respectively. Note that for growing/decaying waves the two amplitude ratios are complex conjugates of each other—see (17)–(19)—so that growing and decaying waves have the same modulus of the amplitude ratio.

To gain some physical insight into the results derived above, we will adopt the same line of reasoning as Bretherton [(1966b); see also Hoskins et al. (1985)] and show that the potential vorticity view may help us to understand the instability mechanism. For this, we rewrite (16) as

$$\omega\cos\phi_C^1 = U^1(\phi_C^1) - Z^{11}(\phi_C^1) - \frac{\epsilon^2}{\epsilon^1}Z^{12}(\phi_C^1), \tag{21a}$$

$$\omega\cos\phi_C^2 = U^2(\phi_C^2) - Z^{22}(\phi_C^2) - \frac{\epsilon^1}{\epsilon^2}Z^{21}(\phi_C^2). \tag{21b}$$

These expressions show that for both the upper and lower waves the complex phase velocity $\omega\cos\phi_C^i$ consists of three contributions. The first contribution is merely due to the advection of the wave pattern by the local basic wind field, being $U^1(\phi_C^1)$ in layer 1 and $U^2(\phi_C^2)$ in layer 2. The second contribution is due to the self-induced motion of the wave pattern similar to that of ordinary (nongrowing) Rossby waves. Material conservation of potential vorticity implies that a zonal contour perturbed with a sinusoidal wave can be represented by a pattern of potential vorticity anomalies of alternating sign around a latitude circle. This perturbation potential vorticity field induces a meridional velocity field that is exactly one-quarter wavelength out of phase with the corresponding displacement field. As a result, the wave will either move westward ($\Delta q^i > 0$) or eastward ($\Delta q^i < 0$) with respect to the local basic zonal flow, but the wave amplitude is not affected. Indeed, both Z^{11} and Z^{22} are real and therefore do not contribute to ω_I. The third contribution reflects the interaction between the upper and the lower waves, which can be explained by considering again the pattern of potential vorticity anomalies. That is, the perturbation potential vorticity fields not only induce a meridional velocity field in the same layer but also a (weaker) meridional velocity field in the other layer that may affect both the real and imaginary parts of the angular phase velocity ω. The contribution to the real part of ω may reinforce or weaken the zonal phase velocities, whereas the contribution to the imaginary part of ω may induce either growth or decay of the wave amplitudes. As stated before, growing/decaying waves require a phase shift between the upper and lower waves. If the jumps in potential vorticity Δq^1 and Δq^2 have opposite signs, this phase shift enables the meridional velocity in layer 1 induced by the perturbed contour in layer 2 to correlate positively or negatively with the meridional displacement of the contour in layer 1, and vice versa. This possibility of positive feedback is the essence of baroclinic growth. Maximum (positive or negative) correlation is obtained when the waves are precisely one-quarter wavelength out of phase, in which case each wave does not affect the zonal phase velocity of the

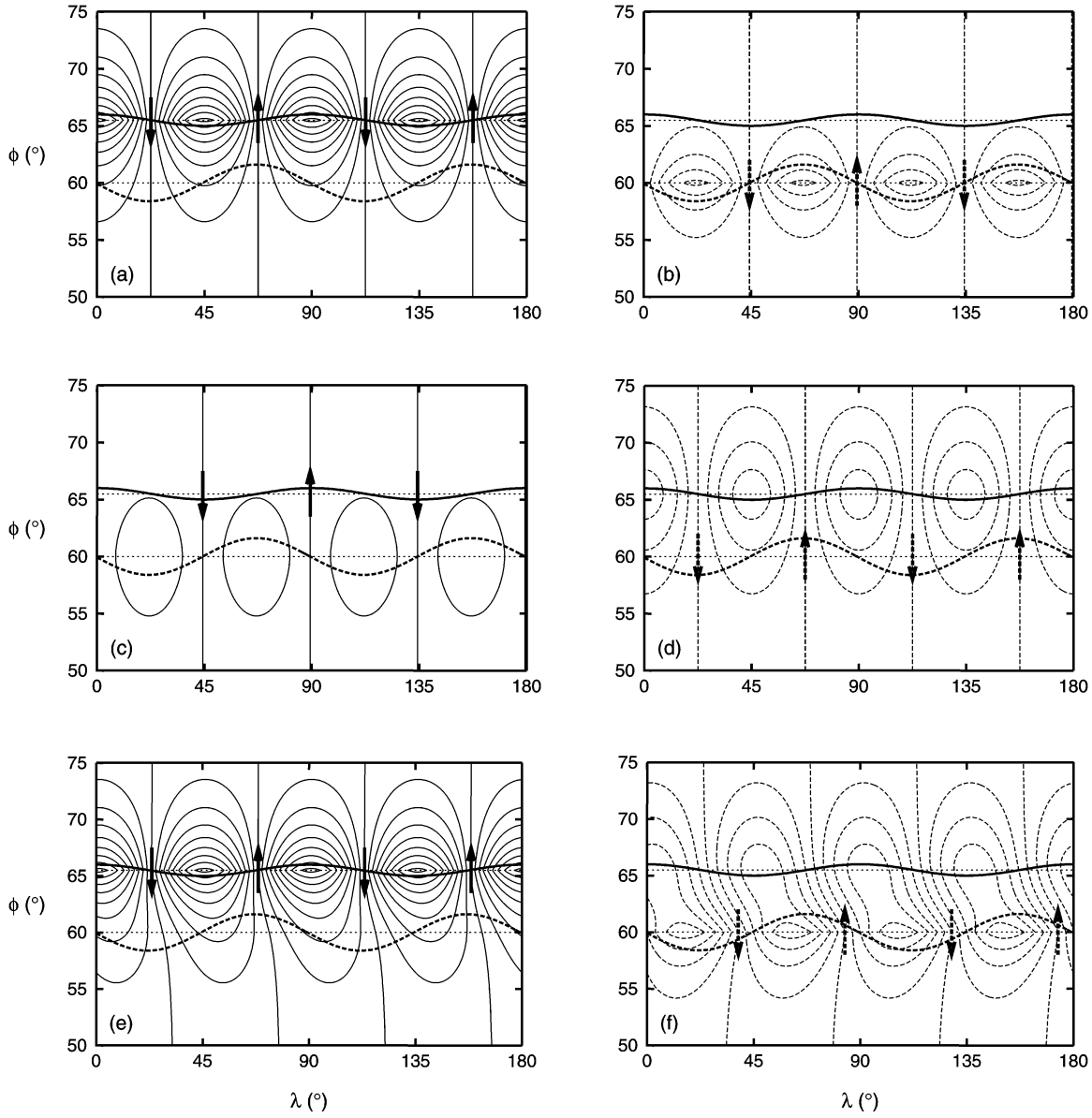

FIG. 4. Streamfunctions associated with infinitesimally small sinusoidal perturbations of the basic-state zonal contours located at $\phi_C^1 = 65.5°$ and $\phi_C^2 = 60.0°$ with $\Delta q^1 = 2.5$, $\Delta q^2 = -0.5$, $|\epsilon^2/\epsilon^1| = 3.2$, and $\arg(\epsilon^2/\epsilon^1) = 92.8°$. Contributions to layers 1 and 2 are indicated by solid and dashed lines, respectively. The heavy solid and heavy dashed contours around $\phi = 65.5°$ and $\phi = 60.0°$ correspond to the perturbed fronts in layers 1 and 2, respectively. The arrows indicate the positions of the maximum northward and southward velocities at the perturbed fronts in layers 1 and 2. (a), (b) The self-induced streamfunction contributions; (c), (d) the perturbation streamfunction induced by the front in the other layer; (e), (f) the total perturbation streamfunction. The contour interval is 0.01, except for (c), for which the contour interval is 0.005.

other wave—see (21) and note that when $\arg(\epsilon^2/\epsilon^1) = 90°$, the ratio ϵ^2/ϵ^1 is purely imaginary—so that the waves propagate in the zonal direction with the zonal phase velocity that they would have in isolation.

As an example, we consider a pair of growing baroclinic waves with wavenumber $m = 4$ on a basic zonal flow with the potential vorticity jumps $\Delta q^1 = 2.5$ and $\Delta q^2 = -0.5$ located at $\phi_C^1 = 65.5°$ and $\phi_C^2 = 60.0°$, respectively. The amplitude of the upper wave, ϵ^1, is arbitrarily set to 0.5°, whereas the amplitude and the phase of the lower wave are calculated from (19), yielding $|\epsilon^2/\epsilon^1| = 3.2$ and $\arg(\epsilon^2/\epsilon^1) = 92.8°$ for growing waves. The basic zonal wind field can be seen in Fig. 3b. In Figs. 4a and 4b we show for each layer the perturbation streamfunction induced by the pattern of potential vorticity anomalies in the same layer, whereas in Figs. 4c and 4d we show for each layer the contribution of the pattern of potential vorticity anomalies in the

other layer. The total perturbation streamfunctions $\delta\psi^1$ and $\delta\psi^2$ are displayed in Figs. 4e and 4f, respectively. In each panel, the heavy solid contour around $\phi = 65.5°$ represents the perturbed front in layer 1, whereas the heavy dashed contour around $\phi = 60.0°$ corresponds to the perturbed front in layer 2. Also indicated for each case are the maximum northward and southward velocities at the perturbed fronts in layers 1 and 2. For clearness only two wavelengths are shown. It can be seen that the maximum northward and southward displacements of each wave are positively correlated with the maximum northward and southward velocities induced by the perturbation vorticity pattern in the other layer, so that the waves will grow. Since the waves are close to one-quarter wavelength out of phase, this correlation is almost maximum while the zonal phase velocity of each wave is virtually unaffected by the meridional velocity induced by the other wave.

In Fig. 5 we consider again a baroclinic wave system with wavenumber $m = 4$. The potential vorticity jumps Δq^1 and Δq^2 are identical to those in the previous case, but the latitude ϕ_C^1 is varied, with ϕ_C^2 fixed at 60.0°. The solutions that correspond to the two roots of ω are indicated by solid and dashed lines. Figure 5a shows the meridional extent of a (growing) wave with unit initial amplitude after a time period of 1 day, that is, $\exp(m\omega_I T_d)$, with $m\omega_I$ the growth rate and $T_d = 2\pi$ a time period of 1 day in units of Ω^{-1}. The waves are unstable for only two specific ranges of latitudes ϕ_C^1 with strong baroclinic instability around $\phi_C^1 = 46.5°$ and $\phi_C^1 = 65.1°$. Indeed, around these latitudes the zonal angular phase velocities of the waves in isolation are approximately equal. The fact that the peaks of maximum growth do not appear symmetrically around $\phi_C^2 = 60.0°$ is due to the sphericity of the earth. As a result, the maximum growth rate occurs at the peak closest to $\phi_C^2 = 60.0°$, for which the induced meridional velocities are larger. Figures 5b–d show the latitudinal variation of the real angular phase velocity ω_R, the modulus of the amplitude ratio ϵ^2/ϵ^1, and the argument of ϵ^2/ϵ^1. Figure 5b shows that the real angular phase velocities ω_R of growing and decaying waves are the same, which are given by the first term in (17). This term is the average of the zonal angular phase velocities that the waves would have in isolation and is represented by the dotted line in Fig. 5b. Note that, at $\phi_C^1 = 46.9°$, the waves have zero zonal phase speed while their amplitudes grow. Neutral waves propagate zonally faster or slower than this average phase velocity [see (17) and (18)]. Likewise, Fig. 5c shows that growing and decaying waves have the same modulus of the amplitude ratio, whereas neutral waves have different amplitude ratios according to (20). The dotted line in Fig. 5c corresponds to the square root of the right-hand side of (20). Figure 5d confirms that a phase shift between the upper and lower waves is a prerequisite for instability to occur.

For each wavenumber m and latitude ϕ_C^1 we calculated

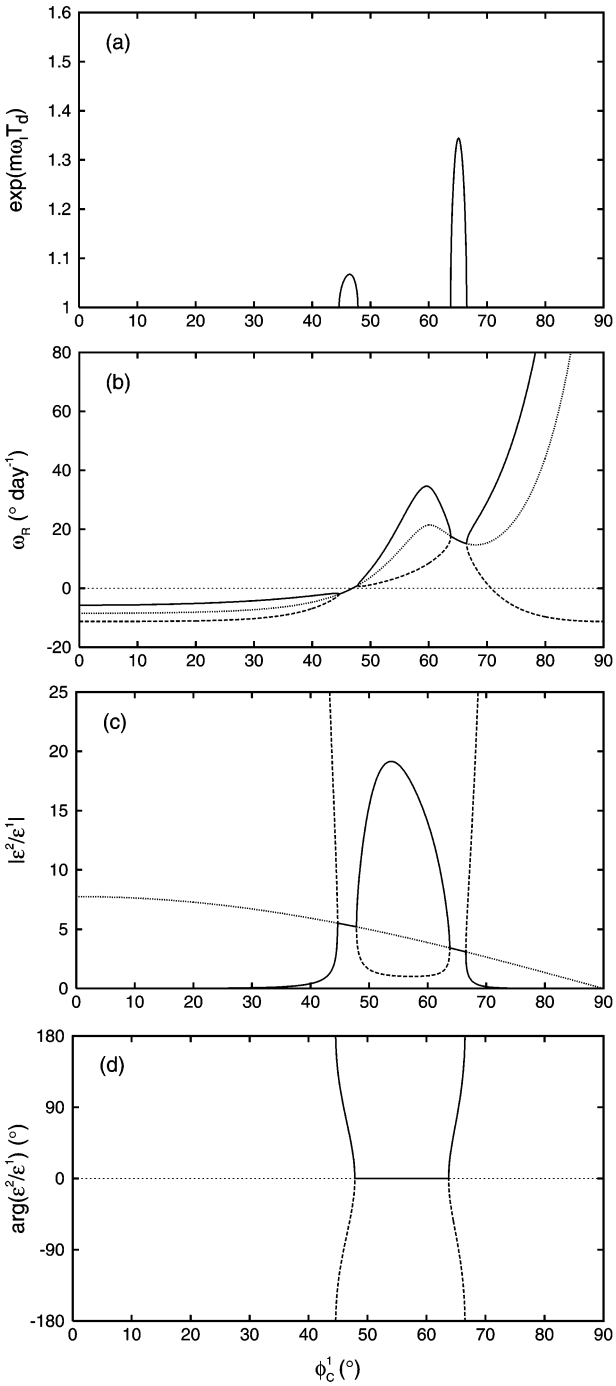

FIG. 5. Several properties of a pair of baroclinic waves, with planetary wavenumber $m = 4$, $\Delta q^1 = 2.5$, and $\Delta q^2 = -0.5$, as a function of ϕ_C^1 with ϕ_C^2 held constant at 60.0°: (a) $\exp(m\omega_I T_d)$, with $m\omega_I$ being the growth rate and $T_d = 2\pi$ being a time period of 1 day in units of Ω^{-1}; (b) the real angular phase velocity ω_R; (c) the modulus of the amplitude ratio ϵ^2/ϵ^1; and (d) the argument of ϵ^2/ϵ^1. The two roots are indicated by the solid and dashed lines. The dotted line in (b) corresponds to the average of the angular phase velocities that the waves would have in isolation, whereas the dotted line in (c) represents the square root of the right-hand side of (20).

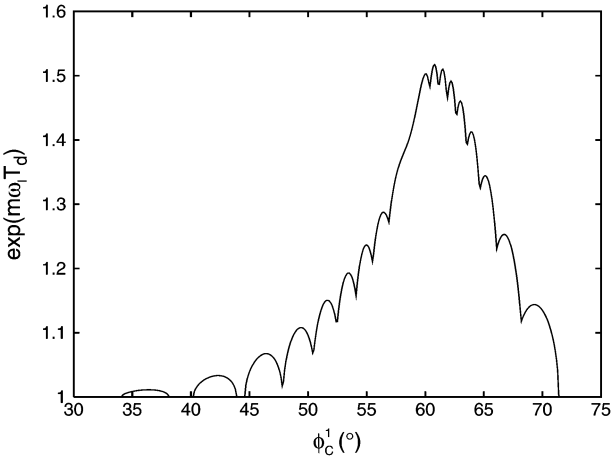

FIG. 6. The maximum growth rate in terms of $\exp(m\omega_I T_d)$ vs ϕ_C^1 with ϕ_C^2 held constant at 60.0°. The potential vorticity jumps are $\Delta q^1 = 2.5$, and $\Delta q^2 = -0.5$.

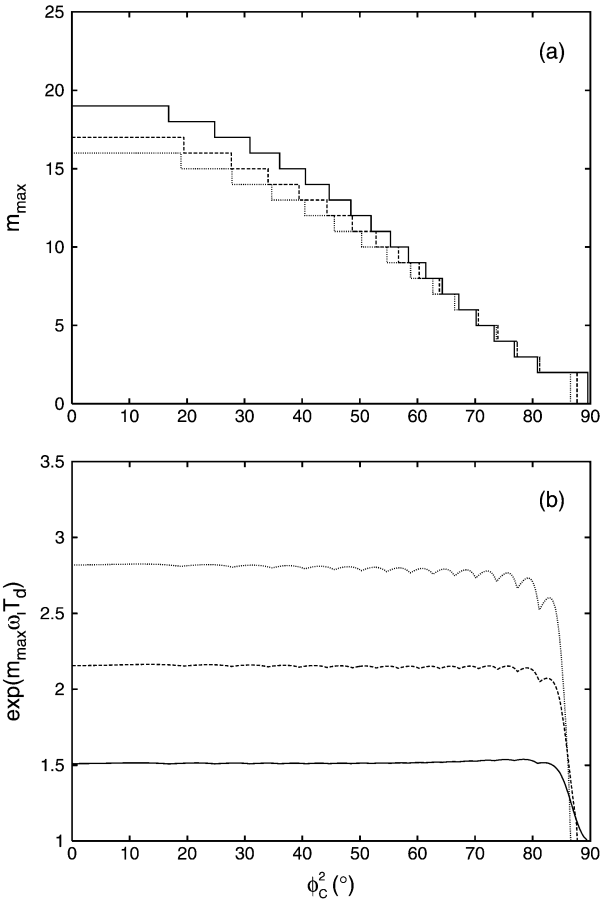

FIG. 7. (a) Planetary wavenumber m_{max} and (b) maximum value of $\exp(m\omega_I T_d)$ vs ϕ_C^2 for $\Delta q^1 = 2.5$ and different values of Δq^2: $\Delta q^2 = -0.5$ (solid line), $\Delta q^2 = -1.5$ (dashed line), and $\Delta q^2 = -2.5$ (dotted line). For each ϕ_C^2 and Δq^2, the latitudinal position of the upper potential vorticity front was varied to find the most unstable wave.

the growth rate $m\omega_I$, with ϕ_C^2 held constant at 60.0°. Figure 6 shows for each latitude ϕ_C^1 the maximum growth rate in terms of the meridional extension of the most unstable wave, with unit initial amplitude, after a time period of 1 day. The curve in Fig. 6 may be considered as the envelope of all the curves that would be obtained by plotting results like Fig. 5a together for all wavenumbers *m.* The instability exists only in limited latitudinal ranges since only discrete values of the planetary wavenumber are allowed by the zonal periodicity of the flow. Each peak corresponds to a different wavenumber *m*, for which the growth rate is maximum. The peaks that are farthest north and south of ϕ_C^2 correspond to $m = 2$, the secondmost-distant peaks correspond to $m = 3$, and so on, until $m = 10$ around ϕ_C^2. Thus, the smaller the meridional distance between the potential vorticity fronts is, the higher is the wavenumber *m* corresponding to maximum growth. This relation between maximum growth rate and planetary wavenumber may be understood from the well-known fact that the induced zonal phase velocities increase with the spatial scale of the wave pattern, a consequence of the so-called scale effect (Hoskins et al. 1985). If the perturbed fronts are moved apart, the difference between the basic zonal velocities $U^1(\phi_C^1)$ and $U^2(\phi_C^2)$ will increase (for example, cf. Figs. 3a and 3b), so that the induced zonal phase velocities should contribute more strongly—that is, longer wavelengths are required for unstable waves to settle down to a common angular phase velocity. Figure 6 reveals that the most unstable waves have wavenumber $m = 9$ and that the corresponding basic-state fronts are located at virtually the same latitudinal position; that is, $\phi_C^1 \approx \phi_C^2$.

We show in Fig. 7a the planetary wavenumber of the wave with maximum growth rate m_{max}, and we show in Fig. 7b the value of this maximum growth rate as a function of ϕ_C^2 for different values of Δq^2. For each ϕ_C^2 and Δq^2, the latitudinal position of the upper wave ϕ_C^1 was varied to find the most unstable wave. The maximum growth rate was found for $\phi_C^1 \approx \phi_C^2$, in agreement with the results in Fig. 6. The planetary wavenumber of the most unstable wave decreases approximately as a cosine of latitude, which suggests that the wavelength of maximum growth is also independent of latitude. The maximum growth rate is nearly independent of latitude, except close to the North Pole. For larger magnitudes of Δq^2 we obtain larger maximum growth rates and smaller planetary wavenumbers m_{max}. The fact that the wavelength of maximum growth is independent of latitude seems to be in disagreement with the instability studies of Charney (1947) and Eady (1949), which show that the wavelength of maximum growth is of the same order as the Rossby radius of deformation, the latter being inversely proportional to the Coriolis parameter f, so that the wavelength of maximum growth is larger at lower latitudes. If this statement also holds for a

latitude-dependent zonal flow with full f^2 dependence on a sphere, the discrepancy between our model results and those of Charney (1947) and Eady (1949) may be due to the assumption $f^2 = 2$ in (6), which makes the Rossby radii of deformation associated with the vertical modes of the two-and-one-half-layer model independent of latitude.

5. Synoptic development

The numerical technique of contour dynamics is applied to investigate whether the two-and-one-half-layer contour dynamics model—with one contour in the upper active layer and another in the lower active layer—is able to produce realistic synoptic development in its nonlinear stage. The linear analysis of the previous section will provide us with an appropriate initial state. A comparison will be made with the evolution of a cutoff cyclone as forecast by a modern global weather prediction model initialized with real atmospheric data.

a. Numerical simulation of a cutoff cyclone

In the appendix it is shown how a general configuration of two contours can be integrated in time using the technique of contour dynamics. The basis of the technique is (A29), which shows how the gradient of the streamfunction—and thus the horizontal velocity—can be calculated by integrating Green's function over the contours. The contours are represented by a finite but adjustable number of nodes that are advected by the local horizontal velocity field. The integration is approximated by a summation over pieces of a great circle connecting the adjacent nodes. [See Verkley (1994) for details, especially his (84)–(88). When the integrand in the calculation of the streamfunction gradient becomes singular, the integral over the pieces of the great circle is evaluated using an analytic expression for the singular part of the integrand.] In general, the contours will be stretched and folded during the flow evolution, so that their length and curvature may increase considerably. Therefore, the number of nodes is allowed to change in time, depending on the degree of deformation of the contours. The nodes are redistributed along the contour using cubic splines between the original nodes. To perform a time integration of complex contour developments, the technique of ''contour surgery'' [for details see Dritschel (1989)] was used in addition to contour dynamics. Surgery removes filamentary structures smaller than a prescribed length scale δ and reconnects contours enclosing the same value of the potential vorticity when the contours get closer than the prescribed length scale. In this respect, small-scale structures are assumed to have a negligible effect on the wind field, which is consistent with the scale effect (Hoskins et al. 1985). That is, the horizontal velocity field (1) follows from the potential vorticity by the inversion of (4), which is insensitive to small-scale features in the potential vorticity field. The surgical scale δ is equal to $\frac{1}{2}\mu^2 L$, where μL is the maximum distance between adjacent nodes and L is a length scale characterizing the overall size of the potential vorticity distribution. The calculations to be discussed below were run with $\mu = 0.05$ and $L = a$, so that $\delta = 1.25 \times 10^{-3} a$. Time integration was performed using a fourth-order Runge–Kutta method with a time step of 1 h. A smaller time step did not significantly affect the time evolution.

Since a full analysis of the evolution of finite-amplitude waves is beyond the scope of this paper, we will focus on a typical example of cyclogenesis, which was selected from a large number of contour dynamics simulations. The initial state is given by a pair of sinusoidal waves with wavenumber $m = 8$ on a basic-state zonal flow defined by $\Delta q^1 = 2.5$, $\Delta q^2 = -2.5$, and $\phi_C^1 = \phi_C^2 = 60.0°$. A meridional cross section of the flow that is associated with this zonal basic state can be seen in Figs. 3c and 3f. The amplitude ratio ϵ^2/ϵ^1 was calculated from (19), yielding $|\epsilon^2/\epsilon^1| = 1.73$ and $\arg(\epsilon^2/\epsilon^1) = 71.6°$ for growing waves. Note that this baroclinic wave system corresponds to maximum growth, which may be verified from Fig. 7a. Other contour dynamics simulations initialized with randomly perturbed zonal contours showed that the most unstable mode became dominant after a while. The initial amplitude ϵ^1 was set to 1.0°. Figure 8 shows the evolution of the upper and lower contours, for days 0–5, where in each panel the upper contour corresponds to the boundary of the shaded region and the lower contour corresponds to the solid line. The initial stage of the evolution is characterized by an exponential growth of the sinusoidal waves (Figs. 8a–c), after which the nonlinear development of the waves becomes apparent. By day 3 (Fig. 8d), the upper-level wave is tilted in the northeast–southwest (NE–SW) direction because of the anticyclonic shear at the southern side of the mean zonal jet, and both fronts advance to lower latitudes in a manner very similar to a dipolar potential vorticity structure. Its self-induced translating motion is caused by the anomalously high and anomalously low potential vorticity regions in the upper and lower layers, respectively. In the final stage (Figs. 8e,f), the tongue of high-potential-vorticity air thins and a cutoff cyclone is formed as the tongue wraps up cyclonically. Note that at day 4 (Fig. 8e) the cyclone is still connected to the polar region by a filament, which could be looked upon as an ''umbilical cord'' (Hoskins et al. 1985; Thorncroft et al. 1993), and whose survivability depends on the surgical scale δ. Indeed, the cyclone shown in Fig. 8f disconnects from the polar region sooner when the simulation is repeated with a larger surgical scale.

It may be worth noting that the cyclogenesis process shown in Fig. 8 falls under the category of an ''LC1'' life cycle, being one of the two paradigms of baroclinic-wave life cycle behavior introduced by Thorncroft et al. (1993). Despite the large number of contour dynamics simulations that we have performed, we have not been

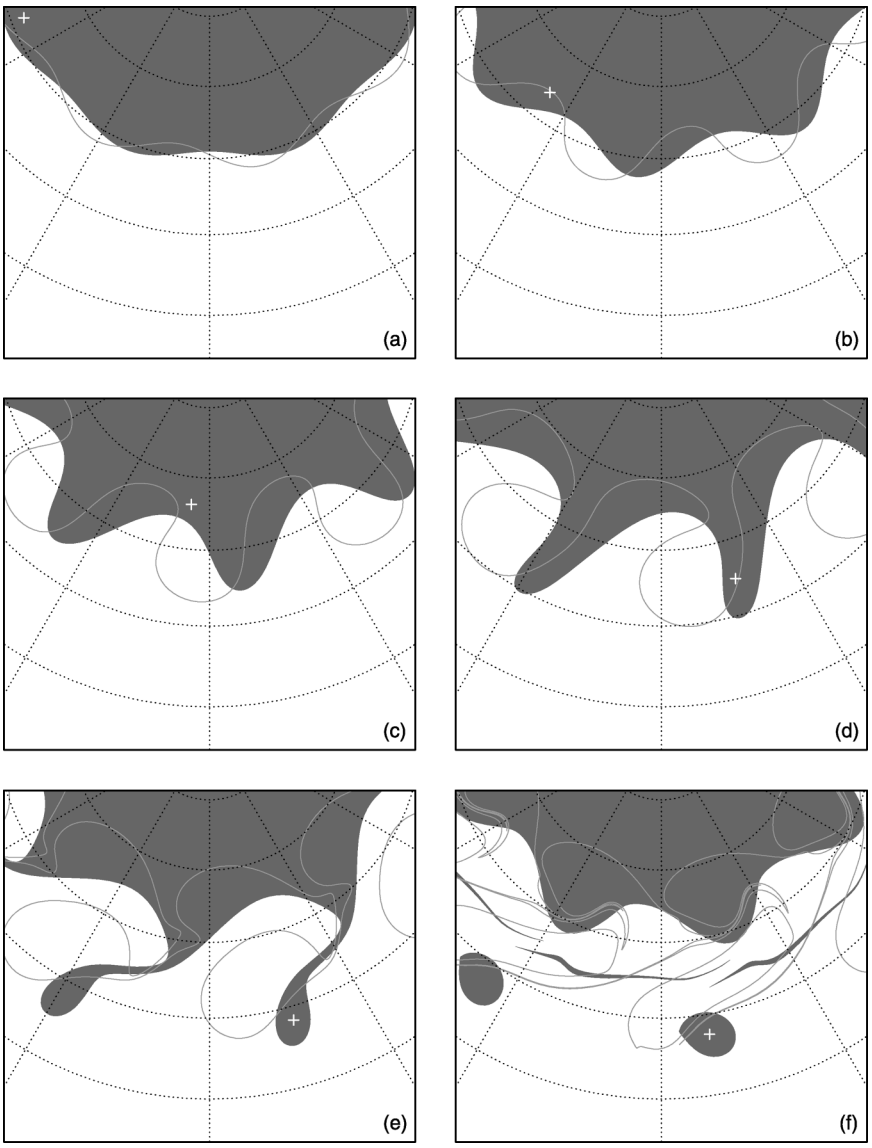

FIG. 8. Evolution of the tropopause (boundary of shaded region) and the polar front (solid line) for days 0–5 (with a 1-day time interval between the panels) as obtained from a two-and-one-half-layer contour dynamics simulation. The initial state corresponds to two zonal potential vorticity fronts at 60.0°N, with $\Delta q^1 = 2.5$ and $\Delta q^2 = -2.5$, which are perturbed with the most unstable sinusoidal wave pattern; that is, $m = 8$, $|\epsilon^2/\epsilon^1| = 1.73$, and $\arg(\epsilon^2/\epsilon^1) = 71.6°$. The initial amplitude $|\epsilon^1|$ was set to 1°. The cross in each frame indicates the instantaneous position of an air column in layer 1 that is finally captured by the cutoff cyclone. Lines of constant longitude and latitude are drawn every 30° and 10°, respectively, with the southernmost grid line corresponding to 40°N.

able to find any example of an LC2 life cycle, whose evolution is dominated by the cyclonic shear on the poleward side of the mean zonal jet. This absence may be due to the fact that in our contour dynamics model only a single contour is used to describe the polar jet stream. As a result, equatorward extensions of a wave in the upper-level polar region are always south of the mean zonal jet and are therefore only affected by the corresponding mean anticyclonic shear, being characteristic of LC1 life cycles. LC2-type evolutions might be possible by introducing more layers and more contours to describe the polar jet stream.

In Fig. 9 we show the same sequence of events as depicted in Fig. 8 but zoomed in on a smaller part of the sphere and a shorter period of time, between day 2.5 and day 5 of the numerical simulation. Instead of the position of the lower potential vorticity front, we show the isolines of the normalized pressure of interface

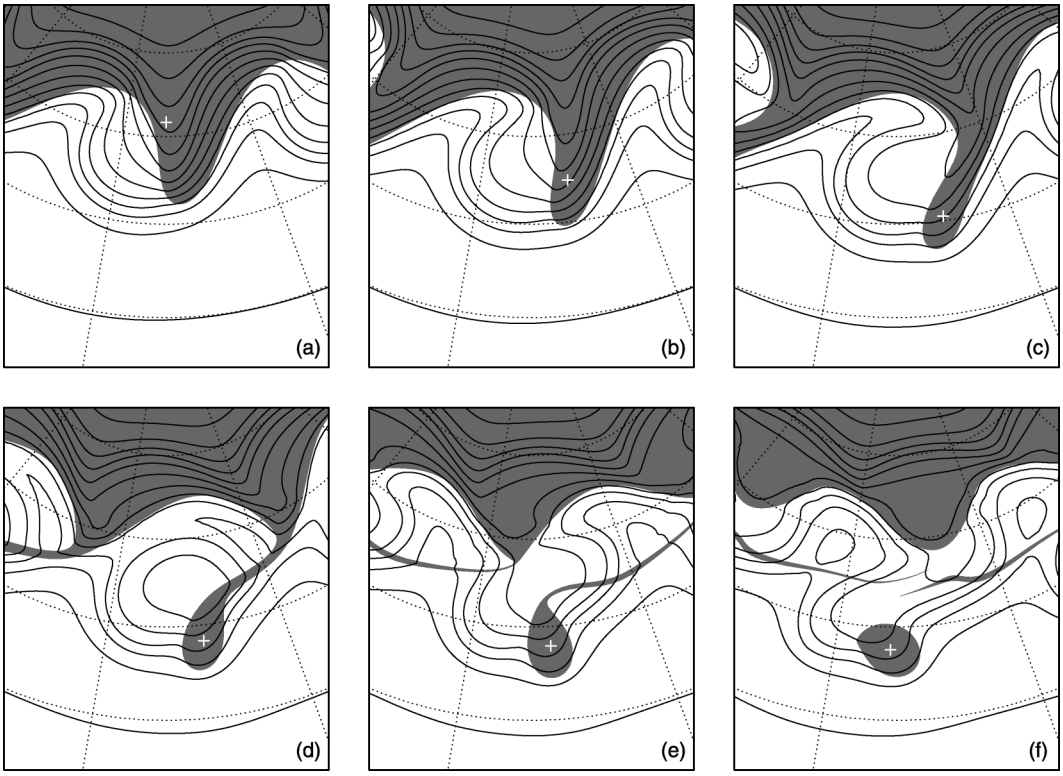

FIG. 9. Evolution of the potential vorticity in layer 1 and the normalized pressure of interface 2 between day 2.5 and day 5, with a 12-h time interval between the panels. The shaded area corresponds to the region of high potential vorticity. The contours correspond to the isolines of the normalized pressure of interface 2 and are drawn every 0.025 units from $\eta_2 = 0.575$ to $\eta_2 = 0.875$ going equatorward. The cross indicates the position of an air column in layer 1. The initial state is the same as in Fig. 8. Lines of constant longitude and latitude are drawn every 30° and 10°, respectively, with the southernmost grid line corresponding to 40°N.

2. The pressure of interface 2 generally decreases when going northward, the steepest gradients occuring around the lower potential vorticity front. This result may be verified by comparing Fig. 8 with Fig. 9 and by looking at the zonal cross sections discussed in section 3. If we would study the flow from the perspective of an isobaric surface with a value in the range of steep change—say, the isobaric surface with normalized pressure 0.775—and would consider the potential temperature on this surface, then the isoline corresponding to the normalized pressure 0.775 will coincide with a discontinuity in potential temperature. Indeed, on this isoline the value of the potential temperature changes from θ^1 to θ^2. This fact implies that if we select an isoline of the normalized interface pressure in the neighborhood of steep change, then this isoline can be looked upon as an isobaric front in potential temperature that closely follows the position of the lower potential vorticity front. This supports our earlier statement that the lower potential vorticity front may be associated with the polar front. However, when the lower potential vorticity front develops much small-scale structure, as happens in the later stages of the numerical simulation, then this association is less clear-cut.

The contour dynamics simulation shown in Fig. 8 was repeated with different values for the potential vorticity jumps while the ratio $\Delta q^2/\Delta q^1$ was retained. Apart from the timing, very similar evolutions were obtained to that shown in Fig. 8. This result may be understood from the fact that the horizontal velocity field $\mathbf{v}$ can be expressed in terms of $\Delta q^2/\Delta q^1$ if $\mathbf{v}$ is scaled either with Δq^1 or Δq^2 and the contribution of the planetary vorticity f to $\mathbf{v}$ is neglected [see (1) and (A29)]. Thus, if the contribution of f to $\mathbf{v}$ is relatively small, which is generally true near the jet axis, baroclinic wave systems with different Δq^i and equal $\Delta q^2/\Delta q^1$ (and otherwise equal basic states) will show virtually the same behavior, although the timescales of their evolutions will differ and will be proportional to Δq^i.

The technique of contour dynamics enables us to calculate the horizontal velocity not only at the positions of the nodes but also at other points in the model atmosphere. Therefore, we can determine the displacement of air tracers, or rather the displacement of air columns, anywhere in the model atmosphere. To calculate the evolution of an air column that ends up in the center of the cutoff cyclone in layer 1, the contour dynamics simulation shown in Fig. 8 was repeated, but

now with the time integration reversed, starting at day 5, and with the center of the cyclone (at 47.5°N and 9.0°E) taken as the initial position of the air column bounded by interfaces 1 and 2 at normalized pressures η_1 and η_2, respectively. Since the positions of the contours were already available every time step from the contour dynamics simulation shown in Fig. 8, we used the corresponding velocity fields to advect the air column backward in time.

Figure 10 shows the time evolution of several quantities for the air column whose instanteneous positions are indicated by the crosses in Figs. 8 and 9. The air entwined into the center of the cyclone appears to originate from polar regions around 61.8°N and 69.2°W. Figure 10a shows the relative vorticity ζ^1, the absolute vorticity $f + \zeta^1$, and the inverse of the column thickness in terms of the normalized pressure, $(\eta_2 - \eta_1)^{-1}$. Figure 10b shows the mean normalized pressure $\frac{1}{2}(\eta_1 + \eta_2)$ and the normalized pressures of the upper and lower boundaries of the air column—that is, η_1 and η_2, respectively. Obviously, both P^1 and θ^1 are constant in time because of the underlying assumptions in section 2. In contrast, both the relative and the absolute vorticity as well as the column thickness change considerably, which is most notable between day 2 and day 4. Close inspection of Fig. 8 reveals that during this time period the air column crosses the lower potential vorticity front (contour in layer 2). As we have seen in section 3, the lower potential vorticity front is accompanied by a distinct change in height of interface 2, which may be verified from the isolines of the normalized pressure of interface 2 depicted in Fig. 9. As a result, the lower boundary of the air column is expected to move downward when it crosses the lower potential vorticity front from the north. Indeed, when we look at the normalized pressure of interface 2 along the trajectory of the air column (Fig. 10b) we see a prominent descent of the column's lower boundary between day 2 and day 4. The upper potential vorticity front is similarly accompanied by a change in height of interface 1, so that the air column's upper boundary moves upward when it approaches the upper potential vorticity front. Since the air column obviously does not cross the upper potential vorticity front, the change in height of interface 1 is less pronounced than that of interface 2. Looking again at the evolution of the normalized pressures at the boundaries of the air column in Fig. 10b, we immediately see the corresponding stretching of the air column within the time period considered. The stretching of the air column is also evident from the evolution of the column thickness, which is inversely proportional to $(\eta_2 - \eta_1)^{-1}$ (see Fig. 10a). Based on the time evolution of the normalized pressures at the boundaries of the air column, we may conclude that the major contribution to the stretching is due to the descent of the lower boundary of the air column when the air column crosses the lower potential vorticity front. Note that during this time period the mean pressure of the air column gradually increases, so that the air column descends in its entirety during its southward motion. Because of the stretching of the air column and the material conservation of potential vorticity, both the relative and absolute vorticity of the air column increase between day 2 and day 4, resulting in a cyclonic wrap-up of the equatorward extension of high-potential-vorticity air and the final formation of a cutoff cyclone. A similar observation was made by Baehr et al. (1999), who found

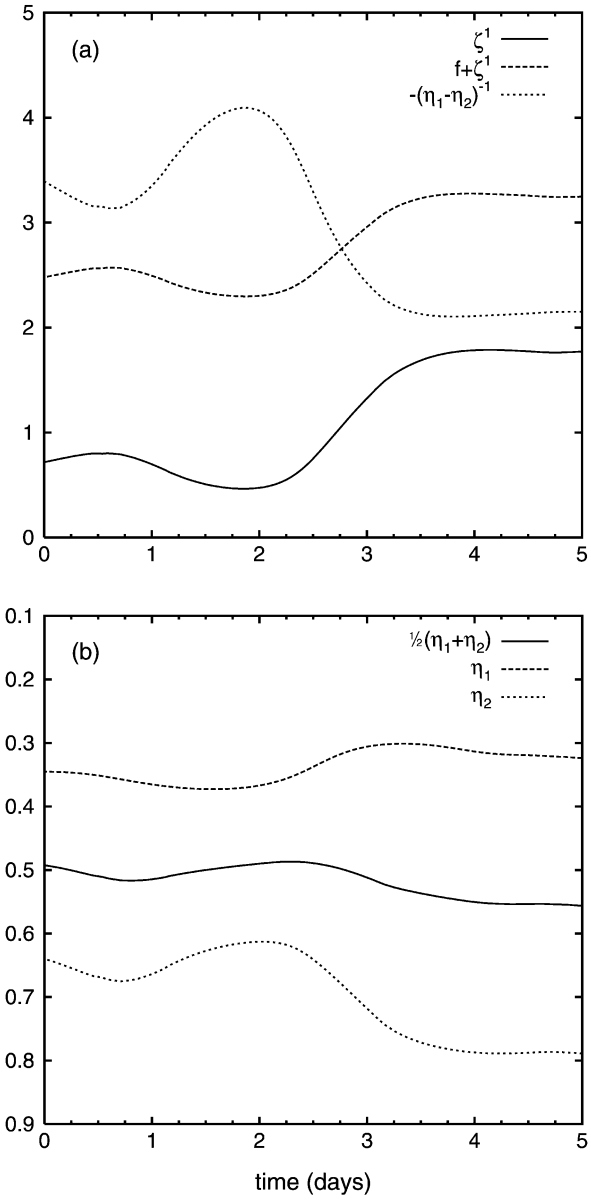

FIG. 10. Time evolution of several quantities for the air tracer shown in Figs. 8 and 9. (top) The relative vorticity ζ^1, the absolute vorticity $f + \zeta^1$, and the inverse of the column thickness in terms of the normalized pressure, $-(\eta_1 - \eta_2)^{-1}$. (bottom) The mean normalized pressure $\frac{1}{2}(\eta_1 + \eta_2)$ and the normalized pressures of the bounding upper and lower interfaces, η_1 and η_2, of the air column.

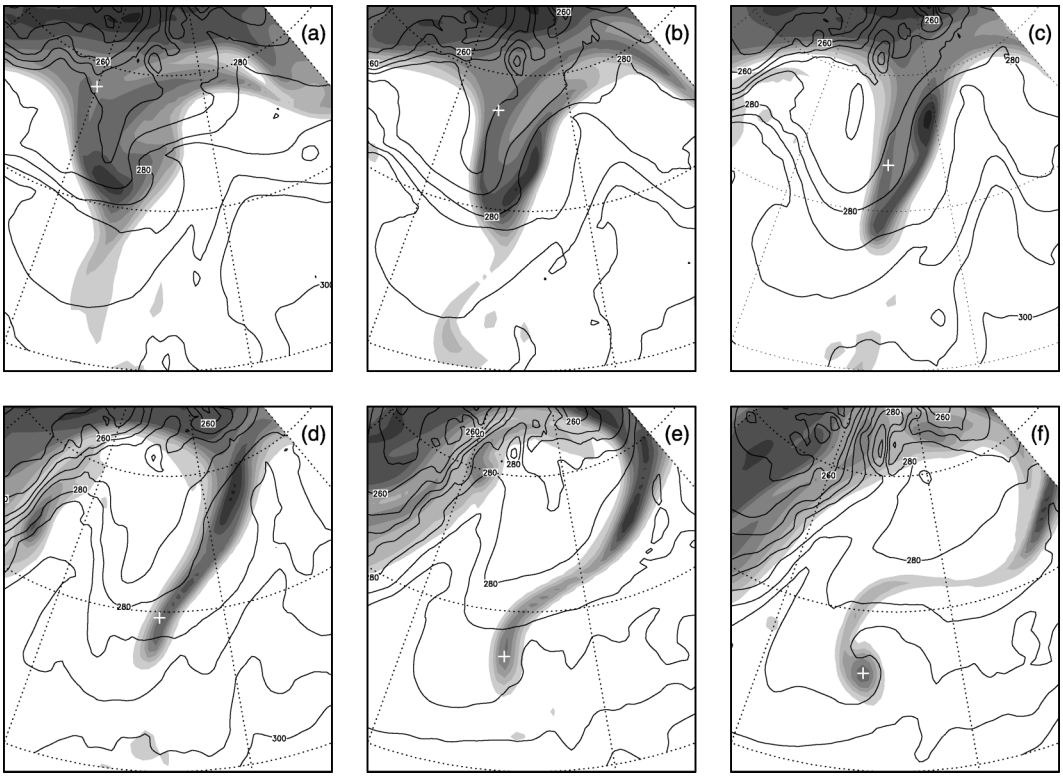

FIG. 11. Evolution of potential vorticity on the 318-K isentropic surface and the potential temperature at model level 28 (approximately 950 hPa) from 0000 UTC 9 Mar to 1200 UTC 11 Mar 1998 (with a 12-h time interval between the panels) based on a 96-h 31-level T213 ECMWF model run, initialized on 1200 UTC 7 Mar 1998. Shaded regions correspond to potential vorticity values larger than 2 PVU, the intensity of which increases every 1 PVU. The isolines of potential temperature are plotted every 5 K. The cross indicates the horizontal position of a tracer that was followed in time with the trajectory model. The lines of constant longitude are drawn every 30° from 90°W to 0°. The lines of constant latitude are drawn every 20° from 20° to 60°N.

that low-level cyclones commonly intensify rapidly as they cross beneath the polar jet stream. Note that the same line of reasoning may be applied to the initial stage of the evolution, between day 0 and day 2, during which the air column resides temporarily on the southern side of the lower potential vorticity front.

b. Observation of a cutoff cyclone

To examine whether the numerical results of Figs. 8–10 have real atmospheric counterparts, we analyzed the development of a North Atlantic cutoff cyclone. The data are based on a 96-h forecast with the global T213 spectral weather prediction model employed by ECMWF. Analyzed fields of 1200 UTC 7 March 1998 were used to initialize the model. The forecast fields were in close agreement with the verifying analyses so that the 96-h model run was a realistic simulation of the actual synoptic development. We used the forecast fields instead of the analyses in order to have a physically consistent dataset in which the modeled quantities are not affected by the addition of new observations. This is essential for the calculation of long-term air tracer movements, which will be discussed later. Figure 11 shows the evolution of potential vorticity on the 318-K isentropic surface for 0000 UTC 9 March 1998 to 1200 UTC 11 March 1998, with a 12-h time interval between the panels. Potential vorticity values larger than 2 potential vorticity units (PVUs) are shaded, with the different shades of gray corresponding to intervals of 1 PVU (PVU is defined as 10^{-6} m^2 s^{-1} K kg^{-1}). Using Reed's (1955) dynamical definition of the tropopause, the shaded regions in Fig. 11 may be associated with the stratosphere. It should be noted that in this case the potential vorticity is defined as $P = -g(f + \zeta_\theta)(\partial\theta/\partial p)$, where P is known as Ertel's potential vorticity for a hydrostatic continuously stratified atmosphere, and ζ_θ is the vertical component of the relative vorticity evaluated on an isentropic surface. The rate of change of Ertel's potential vorticity following adiabatic flow is approximately proportional to the rate of change of quasigeostrophic potential vorticity as defined in section 2 following the horizontal geostrophic wind field (Charney and Stern 1962). The potential vorticity field was calculated by finite differences from the wind, temperature, and pressure fields on a three-dimensional grid with 31

model levels and a horizontal grid spacing of 1° × 1°. Linear interpolation in the vertical direction was used to determine the potential vorticity field on the isentropic surface. Cases in which the potential vorticity was multivalued in the vertical direction—indicative of tropopause folding—or in which the lapse rate was superadiabatic were not observed, so that both the potential vorticity and the potential temperature may be assumed to increase upward. Also shown, every 5 K, are the isolines of potential temperature at model level 28, corresponding to approximately 950 hPa.

At 0000 UTC 9 March 1998 (Fig. 11a), the flow is dominated by a prominent equatorward extension of high-potential-vorticity air above the Atlantic. Over the next 2 days, this region of high potential vorticity thins and is greatly elongated in the NE–SW direction on the southern side of the mean zonal jet, as apparent from Figs. 11b–d. By 0000 UTC 11 March 1998 (Fig. 11e), the southward tip of the filament starts to wrap up cyclonically, and 12 h later (Fig. 11f) some high-potential-vorticity air has been pinched off into the center of the developing cyclone and the cutting-off process is almost complete. The isolines of low-level potential temperature reveal that, on its western side, the equatorward extension of high potential vorticity is accompanied by a southward outflow of cold air, in much the same way as demonstrated by the contour dynamics simulation.

Based on the output of the previous ECMWF model run, the trajectory of a single air tracer was calculated with the trajectory model of Scheele et al. (1996). The crosses in Fig. 11 mark the horizontal positions of the air tracer with a 12-h time interval between them. The advecting velocity field was based on the three-dimensional velocity fields of the ECMWF model run, which were available every 6 h. Velocity fields at intermediate times were obtained by quadratic interpolation, whereas velocities at positions other than the grid points were calculated by bilinear interpolation. The initial tracer position was chosen at the center of the cutoff cyclone at 1200 UTC 11 March 1998 (see Fig. 11f) with $\lambda = 44.8°$W, $\phi = 31.7°$N, and $p = 346$ hPa. The trajectory model was integrated backward in time, with a time step of 10 min, to calculate the subsequent tracer positions. For a detailed description of the method of calculation, the reader is referred to Scheele et al. (1996).

Several quantities were calculated along the trajectory of the air tracer and are presented in Fig. 12, where day 0 corresponds to 1200 UTC 7 March 1998. Figure 12a shows the relative vorticity ζ_θ, the absolute vorticity $f + \zeta_\theta$, the gradient $-\partial\theta/\partial p$, and the potential vorticity P, defined as $P = -g(f + \zeta_\theta)(\partial\theta/\partial p)$. Figure 12b shows the pressure p and the potential temperature θ of the tracer. Focusing on the potential vorticity first, we observe that the potential vorticity fluctuates around 5 PVU with an average time period of 6 h. This result is most likely due to the dependence of potential vorticity on spatial derivatives, which are sensitive to both temporal and spatial interpolation. Indeed, the potential temperature θ fluctuates much less.

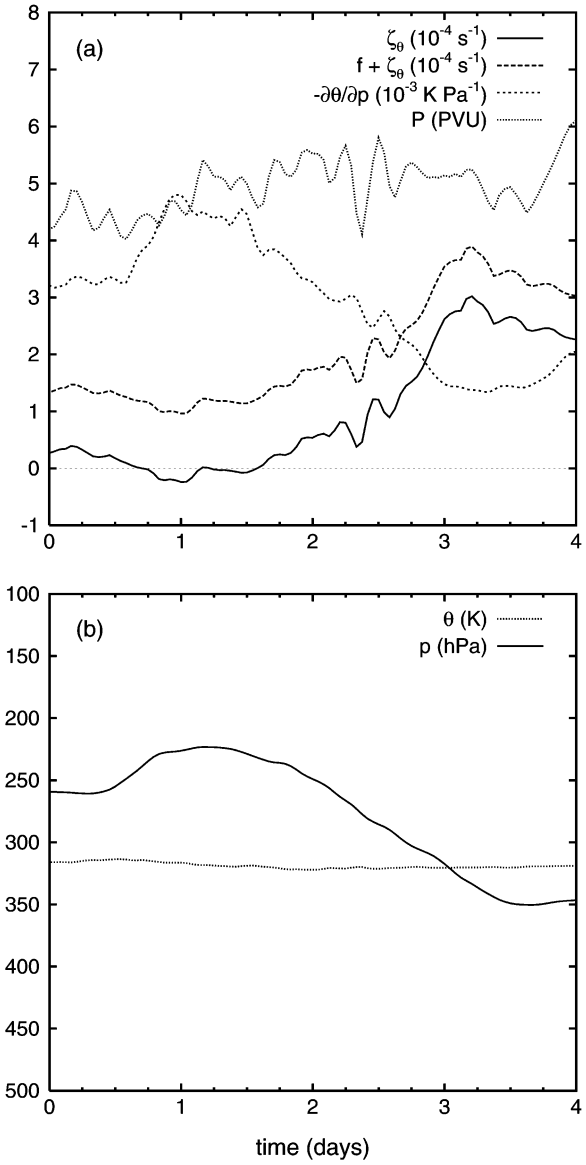

FIG. 12. Time evolution of several quantities for the air tracer shown in Fig. 11, where day 0 corresponds to 1200 UTC 7 Mar 1998. (top) The isentropic relative vorticity ζ_θ, the absolute vorticity $f + \zeta_\theta$, the gradient $-\partial\theta/\partial p$, and the potential vorticity P, defined by $P = -g(f + \zeta_\theta)(\partial\theta/\partial p)$. (bottom) The pressure p and the potential temperature θ of the tracer.

The gradient $-\partial\theta/\partial p$ shows a marked decrease between days 1 and 3, when the upper-air tracer moves closer to the tropopause and overtakes a region of strong potential temperature gradients associated with the polar front. During the same time period, the air tracer moves down from about 225 to 350 hPa. Since P is approximately conserved, both the relative and absolute vorticity show a pronounced increase within this time period. Also note that during the initial stage of the evo-

lution, between days 0 and 1, the air tracer moves poleward toward a region of strong potential temperature gradients at higher latitudes (not shown), which explains the initial increase of $-\partial\theta/\partial p$ and the corresponding decrease of relative and absolute vorticity. A comparison of Figs. 10 and 12 reveals that the contour dynamics model captures the main dynamic characteristics of the ECMWF forecast remarkably well.

6. Summary and conclusions

We have examined synoptic development in an idealized balanced model of the atmosphere, formulated in terms of three layers of uniform potential temperature and two potential vorticity fronts. The upper layer was assumed to have zero velocity and a corresponding flat upper surface. In the lower two active layers, the horizontal structure was represented by a piecewise-uniform distribution of potential vorticity with a single front in each layer. The model atmosphere was assumed to be in hydrostatic and geostrophic balance, in which for the latter a simplification of linear balance was chosen, and diabatic heating/cooling and mechanical forcing/friction were neglected. In addition, the potential vorticity was linearized around the state of rest, so that the potential vorticity inversion problem becomes linear, and the squared Coriolis parameter was replaced by its global average, so that the equations reduce to the familiar quasigeostrophic equations for a layered model.

It was shown that realistic zonal flows can be obtained. The velocity field in the upper active layer is sharply peaked at the upper potential vorticity front and, depending on the choice of parameters, this is also true for the velocity field in the lower active layer. The thickness of the upper active layer increases rapidly at the upper potential vorticity front when going from pole to equator. As a result, meridional cross sections show the upward and downward bowing of the interface heights that is characteristic for isentropes around the jet stream. The front in the upper layer was therefore associated with the tropopause or, rather, with the sudden increase in height of the tropopause: the ''tropopause break.'' The potential vorticity front in the lower layer was seen to enhance the downward bowing of the lower interface and to add to the baroclinicity of the system. For this reason, the lower potential vorticity front was associated with the polar front.

By analyzing the linear dynamics of infinitesimal wavelike perturbations of zonal contours it was possible to expose the physical nature of the instability mechanism in a clear way. Our analysis was in effect an application of the potential vorticity view of baroclinic instability as advocated by Bretherton (1996a,b) and Hoskins et al. (1985) because perturbations of the contours are directly related to perturbations of the potential vorticity field. By studying the streamfunction and meridional velocity fields that the perturbations of one front induce at the other, it could be seen that positive feedback and associated wave growth is only possible when there is a phase shift between the two waves: in this case the meridional velocity field that one front induces at the other correlates positively with the meridional displacements of the contours. For waves of a given planetary wavenumber and a fixed position of one of the fronts, wave growth is only possible within limited ranges of the position of the other front. The maximum growth rates and highest planetery wavenumbers are found for potential vorticity fronts that are located at approximately the same latitude.

The model's ability to produce realistic synoptic development was investigated by the analysis of a typical contour dynamics simulation during which a portion of high potential vorticity in the upper active layer pinched off and formed a cutoff cyclone. The results are remarkably consistent with the evolution of an observed cutoff cyclone as simulated by the ECMWF forecast model initialized with real atmospheric data. This similarity was evident from the marked NE–SW tilt of the thinning upper-level trough, the subsequent formation of a southward-moving dipolar potential vorticity structure, and the final cyclonic wrap-up stage, which resulted in the cutoff cyclone. Several properties were calculated along the trajectory of an air tracer that was eventually captured by the cutoff cyclone. Again, a striking similarity was found between the contour dynamics results and the evolution simulated by the ECMWF model initialized with real atmospheric data. In both cases the air tracers originated from much higher latitudes. The equatorward migration of the air tracers was associated with descending motion as well as vertical stretching, resulting in a prominent increase of relative and absolute vorticity due to the (approximate) conservation of potential vorticity. An explanation for the observed stretching was found from the contour dynamics simulations by looking at the positions of the layer interfaces along the parcel's trajectory. The major amount of stretching occurs when the air parcel crosses the lower potential vorticity front associated with the polar front.

Despite the model's crude discretization in terms of only three isentropic layers—of which the upper one is passive—and only two regions of uniform potential vorticity in each active layer, the results obtained carry over to the real atmosphere. Indeed, the two fronts in the model are associated with two important structural elements that dominate the atmospheric circulation: the tropopause and the polar front. The model's assumption of hydrostatic and geostrophic balance as well as the neglect of diabatic heating/cooling and mechanical forcing/friction is not unreasonable and is nearly satisfied by the real atmosphere as long as the spatial scale is not too short and the timescale is not too long. By building upon these basic principles, we enabled ourselves to concentrate fully on the potential vorticity structure as determined by the two fronts and its time evolution as determined by the advection of the fronts. This ap-

proach has proven advantageous, not only in the linear analysis of small-amplitude waves but also in understanding the subsequent nonlinear stages of synoptic development.

There are several ways to proceed. First of all it is necessary to explore more fully the range of possible parameters of the model and the way in which these parameters determine the model's evolution. For future applications, it might turn out to be necessary to relieve the model from some of its limitations. The accuracy of the model could be improved by allowing for a full f^2 dependence of the system parameters and by abandoning the linearization of potential vorticity around the state of rest. As remarked before, the assumption of no latitude dependence of the system parameters means that vortex-tube stretching and squeezing are effectively independent of latitude, which seems unrealistic with regard to the classical instability studies by Charney (1947) and Eady (1949). The linearization is restrictive because it implies that the variations in interface pressures have to be small with respect to their average values. It might also be worthwhile to use the more accurate expression for the balanced horizontal velocity that can be derived using Salmon's method [see Verkley (2001) and references therein for details]. In addition, better resolution of the vertical and horizontal structure, that is, more layers and more contours, might be necessary to describe more realistic potential vorticity structures. For example, it would be very interesting to see whether both paradigms of baroclinic-wave life cycle behavior introduced by Thorncroft et al. (1993) can be reproduced by such an improved model. Application of the contour-advective semi-Lagrangian algorithm developed by Dritschel and Ambaum (1997) could alleviate the problem of the necessarily increased computational effort.

Acknowledgments. We are grateful to Dr. David Dritschel for providing the source code of the contour surgery algorithm and to Mr. Rinus Scheele and Dr. Peter Siegmund for performing numerical simulations with the trajectory model. We also thank Dr. Aarnout van Delden and two anonymous reviewers whose criticism and suggestions have clarified the physical interpretation of the model. One of the authors (RRT) gratefully acknowledges financial support by the Council for Earth and Life Sciences (ALW) of the Netherlands Organization for Scientific Research (NWO).

APPENDIX

Mathematical Details

a. Linearization of P around the state of rest

To linearize the potential vorticity P around the state of rest, the definition of $P^i = (f + \zeta^i)/(\eta_{i+1} - \eta_i)$ in layer i is rewritten as

$$P^i = \left(\frac{f}{\overline{\eta}_{i+1} - \overline{\eta}_i}\right)\left(1 + \frac{\zeta^i}{f}\right) \times \left[\frac{\overline{\eta}_{i+1}}{\overline{\eta}_{i+1} - \overline{\eta}_i}\left(1 + \frac{\eta'_{i+1}}{\overline{\eta}_{i+1}}\right) - \frac{\overline{\eta}_i}{\overline{\eta}_{i+1} - \overline{\eta}_i}\left(1 + \frac{\eta'_i}{\overline{\eta}_i}\right)\right]^{-1}. \tag{A1}$$

We will assume that ζ^i/f, $\eta'_i/\overline{\eta}_i$, and $\eta'_{i+1}/\overline{\eta}_{i+1}$ are small compared to 1 so that we can linearize the product of the second and third factor. We then obtain approximately

$$P^i = \left(\frac{1}{\overline{\eta}_{i+1} - \overline{\eta}_i}\right)\left(f + \zeta^i - f\frac{\overline{\eta}_{i+1}}{\overline{\eta}_{i+1} - \overline{\eta}_i}\frac{\eta'_{i+1}}{\overline{\eta}_{i+1}} + f\frac{\overline{\eta}_i}{\overline{\eta}_{i+1} - \overline{\eta}_i}\frac{\eta'_i}{\overline{\eta}_i}\right), \tag{A2}$$

which can be written in terms of the streamfunction ψ^i by realizing that $\zeta^i = \nabla^2\psi^i$ and that the interface pressures η_i are related to the Montgomery potentials M^i by

$$M^0 = M^1 + c_p(\theta^0 - \theta^1)\eta_1^\kappa, \tag{A3a}$$

$$M^1 = M^2 + c_p(\theta^1 - \theta^2)\eta_2^\kappa, \tag{A3b}$$

$$M^2 = c_p\theta^2\eta_3^\kappa. \tag{A3c}$$

Relations (A3a) and (A3b) can be derived by applying the definition of the Montgomery potential infinitely close to both sides of interface 1 and 2, respectively, whereas relation (A3c) follows directly from the definition of the Montgomery potential and the condition $z_3 = 0$. In each case, the definition of potential temperature was used to express the absolute temperatures in terms of the normalized pressures. Using $M^i = \overline{M}^i + f\psi^i$ and $\eta_i = \overline{\eta}_i + \eta'_i$ together with (A3) and assuming $\eta'_i/\overline{\eta}_i \ll 1$, we find the relations between the pressure deviations at the interfaces and the streamfunctions in the layers:

$$f\psi^0 = f\psi^1 + \kappa c_p\overline{\eta}_1^{\kappa-1}(\theta^0 - \theta^1)\eta'_1, \tag{A4a}$$

$$f\psi^1 = f\psi^2 + \kappa c_p\overline{\eta}_2^{\kappa-1}(\theta^1 - \theta^2)\eta'_2, \tag{A4b}$$

$$f\psi^2 = \kappa c_p\overline{\eta}_3^{\kappa-1}\theta^2\eta'_3. \tag{A4c}$$

Substitution of (A4) and $\zeta^i = \nabla^2\psi^i$ into (A2) then gives

$$P^i = \frac{q^i}{\overline{\eta}_{i+1} - \overline{\eta}_i}, \tag{A5}$$

where the fields q^i are related to the streamfunction by

$$q^0 = f + \nabla^2\psi^0 - F_l^0(\psi^0 - \psi^1), \tag{A6a}$$

$$q^1 = f + \nabla^2\psi^1 + F_u^1(\psi^0 - \psi^1) - F_l^1(\psi^1 - \psi^2), \tag{A6b}$$

$$q^2 = f + \nabla^2\psi^2 + F_u^2(\psi^1 - \psi^2) - F_l^2\psi^2, \tag{A6c}$$

with F_l^i and F_u^i being the parameters defined in (6). Expressions for the interface heights z_i and their per-

turbations z_i', which are very similar to (A3) and (A4), can be found by evaluating the Montgomery potential at the lower and upper interface of each layer *i*. It is seen easily that, by evaluating M^0 at the upper system boundary where $\eta_0 = 0$, we have $M^0 = gz_0$. A passive upper layer means therefore that z_0 is constant or $\psi^0 = 0$. Taking $\psi^0 = 0$ in (A6) leads to the expressions (4)–(7).

b. Contour dynamics

To find a solution of the streamfunction ψ^i in each active layer ($i = 1, 2$), we rewrite (4) as

$$\nabla^2\psi^i - \sum_j F^{ij}\psi^j = \sigma^i, \tag{A7}$$

where the indices i and j assume the values 1 and 2. The source terms σ^i represent the perturbation or anomalous potential vorticity with respect to the rest state $\overline{q}^i = f$; thus, $\sigma^i = q^i - f$. Let χ^{ik}, for $k = 1$ and $k = 2$, be the normalized eigenvectors, and $\tilde{F}^k$ be the corresponding eigenvalues of the matrix of parameters F^{ij}; that is,

$$\sum_j F^{ij}\chi^{jk} = \tilde{F}^k\chi^{ik}, \tag{A8}$$

for $k = 1, 2$. According to Wilkinson (1965), because F^{ij} is a quasi-symmetric tridiagonal matrix (in our case a matrix with real diagonal elements and off-diagonal elements satisfying $F^{21}F^{12} > 0$), the matrix is nonsingular with real, nonnegative eigenvalues and real eigenvectors. As a result, the streamfunction and source term in layer i can always be written as a sum over the eigenvectors χ^{ik}; that is,

$$\psi^i = \sum_k \chi^{ik}\tilde{\psi}^k, \qquad \sigma^i = \sum_k \chi^{ik}\tilde{\sigma}^k, \tag{A9}$$

and likewise for all other dynamical fields. The coefficients $\tilde{\psi}^k$ and $\tilde{\sigma}^k$ are the projections of ψ^i and σ^i onto the kth vertical mode, of which the vertical structure is given by the eigenvector χ^{ik}. Conversely, the streamfunction and source term associated with mode k can be written as a sum over the active layers ($i = 1, 2$); that is,

$$\tilde{\psi}^k = \sum_i \tilde{\chi}^{ki}\psi^i, \qquad \tilde{\sigma}^k = \sum_i \tilde{\chi}^{ki}\sigma^i, \tag{A10}$$

where $\tilde{\chi}^{jk}$, for $j = 1$ and $j = 2$, are the orthonormal counterparts of the eigenvectors, namely, $\Sigma_i \tilde{\chi}^{ki}\chi^{im} = \delta_{km}$ and $\Sigma_k \chi^{ik}\tilde{\chi}^{kj} = \delta_{ij}$. The eigenvectors χ^{ik} and their orthonormal counterparts $\tilde{\chi}^{kj}$ are similar to the vertical structure functions satisfying the Sturm–Liouville equation in a continuously stratified atmosphere.

Projecting (A7) onto the kth vertical mode gives

$$\nabla^2\tilde{\psi}^k - \tilde{F}^k\tilde{\psi}^k = \tilde{\sigma}^k, \tag{A11}$$

which can be derived easily by substituting expressions (A9) into (A7), and by making use of (A8) and the orthogonality properties of the eigenvectors. As expressed by (A10), the source field $\tilde{\sigma}^k$ is the projection of the anomalous potential vorticity σ^i on the kth vertical mode. Equation (A11) is an inhomogeneous Helmholtz equation, $\nabla^2 - \tilde{F}^k$ being the Helmholtz operator acting on $\tilde{\psi}^k$. This operator is mathematically identical with the corresponding operator in the equivalent barotropic vorticity equation. In that equation $\tilde{F}^k\tilde{\psi}^k$ is the so-called Cressman term that allows for vortex-tube stretching and squeezing (Cressman 1958). As a result, the motion related to the kth vertical mode is identical to the motion in an isentropic layer with height $2\Omega^2a^2/(\kappa g\tilde{F}^k)$.

The solution of (A11) is given by an integral over the whole sphere of the Green's function $\tilde{G}^k$ multiplied by the source field $\tilde{\sigma}^k$:

$$\tilde{\psi}^k(\mathbf{r}) = \int_S dS'\tilde{G}^k(\mathbf{r};\,\mathbf{r}')\tilde{\sigma}^k(\mathbf{r}'), \tag{A12}$$

where S denotes the spherical surface, and $dS' = d\lambda'\,d\phi'\cos\phi'$ is a spherical surface element. Here, $\mathbf{r}$ refers to a field point with coordinate (λ, ϕ), and $\mathbf{r}'$ refers to the source point with coordinate (λ', ϕ'). The Green's function $\tilde{G}^k$ of the Helmholtz operator $\nabla^2 - \tilde{F}^k$ is a solution of the equation

$$\nabla^2\tilde{G}^k(\mathbf{r};\,\mathbf{r}') - \tilde{F}^k\tilde{G}^k(\mathbf{r};\,\mathbf{r}') = \delta(\mathbf{r};\,\mathbf{r}'), \tag{A13}$$

with the Dirac delta function $\delta(\mathbf{r};\,\mathbf{r}')$ as a source. In Verkley (1994) it is shown that the Green's function $\tilde{G}^k$ is given by

$$\tilde{G}^k(\mathbf{r};\,\mathbf{r}') = -[4\cosh(\pi\gamma^k)]^{-1}P^0_{-1/2+i\gamma^k}(-\cos\theta''), \tag{A14}$$

where $P^m_\nu(x)$ is a Legendre function with integer order m, real or complex degree ν, and real argument x. The order of the Legendre function is 0, whereas the degree is given by $-\frac{1}{2} + i\gamma^k$. The parameter γ^k is real and is related to $\tilde{F}^k$ by $\tilde{F}^k = \frac{1}{4} + (\gamma^k)^2$. The angular distance θ'' between the points $\mathbf{r}$ and $\mathbf{r}'$ follows from the cosine rule of spherical trigonometry: $\cos\theta'' = \sin\phi\sin\phi' + \cos\phi\cos\phi'\cos(\lambda - \lambda')$.

From the streamfunction of mode k at field point $\mathbf{r}$, we can find the streamfunction in layer i at point $\mathbf{r}$ by the linear combination given by (A9). That is, substitution of (A12) into (A9) and using (A10) gives an expression for ψ^i in terms of the source field:

$$\psi^i(\mathbf{r}) = \sum_j \int_S dS'G^{ij}(\mathbf{r};\,\mathbf{r}')\sigma^j(\mathbf{r}'), \tag{A15}$$

where

$$G^{ij}(\mathbf{r};\,\mathbf{r}') = \sum_k \chi^{ik}\tilde{G}^k(\mathbf{r};\,\mathbf{r}')\tilde{\chi}^{kj} \tag{A16}$$

relates the contribution of the source field in layer j to the streamfunction in layer i. Using (A8), (A13), and (A16), we can derive that G^{ij} is a solution of

$$\nabla^2 G^{ij}(\mathbf{r};\,\mathbf{r}') - \sum_n F^{in} G^{nj}(\mathbf{r};\,\mathbf{r}') = \delta_{ij}\delta(\mathbf{r};\,\mathbf{r}'), \quad \text{(A17)}$$

which should be compared with expression (A13).

In each active layer we now define two regions of uniform potential vorticity according to (8). It may be verified using (A9), (A10), and (A11) that for this distribution of potential vorticity, expression (A15) for the streamfunction becomes

$$\psi^i(\mathbf{r}) = \sum_{jk} \chi^{ik}\tilde{\chi}^{kj}\left[-\frac{q_0^j}{\tilde{F}^k} + \frac{f(\mathbf{r})}{\tilde{F}^k + 2} + \Delta q^j \xi^{jk}(\mathbf{r})\right], \quad \text{(A18)}$$

where the field $\xi^{jk}(\mathbf{r})$ is a solution of

$$\nabla^2 \xi^{jk}(\mathbf{r}) - \tilde{F}^k \xi^{jk}(\mathbf{r}) = \mathcal{H}^j(\mathbf{r}), \quad \text{(A19)}$$

that is, is a solution of the inhomogeneous Helmholtz equation with $\mathcal{H}^j(\mathbf{r})$ as the source term. A general solution of this equation is given by the following integral:

$$\begin{aligned}\xi^{jk}(\mathbf{r}) &= \int_S dS' \tilde{G}^k(\mathbf{r};\,\mathbf{r}')\mathcal{H}^j(\mathbf{r}') \\ &= \int_{R_1^j} dS' \tilde{G}^k(\mathbf{r};\,\mathbf{r}'), \quad \text{(A20)}\end{aligned}$$

where $\tilde{G}^k(\mathbf{r};\,\mathbf{r}')$ is Green's function of the Helmholtz operator, that is, a function satisfying (A13). Substitution of (A20) into (A18) yields

$$\psi^i(\mathbf{r}) = \sum_{jk} \chi^{ik}\tilde{\chi}^{kj}\left[-\frac{q_0^j}{\tilde{F}^k} + \frac{f(\mathbf{r})}{\tilde{F}^k + 2} + \Delta q^j \int_{R_1^j} dS' \tilde{G}^k(\mathbf{r};\,\mathbf{r}')\right]. \quad \text{(A21)}$$

The essence of contour dynamics is that the system can be integrated in time by advecting the contours with the local velocity, so that we have a closed dynamical system for fluid particles that lie on the contours. This system is generally referred to as a ''contour dynamics system.'' The horizontal velocity field (1) follows from the gradient of ψ^i, for which the previous expression gives

$$\nabla\psi^i(\mathbf{r}) = \sum_{jk} \chi^{ik}\tilde{\chi}^{kj}\left[\frac{\nabla f(\mathbf{r})}{\tilde{F}^k + 2} + \Delta q^j \int_{R_1^j} dS' \nabla \tilde{G}^k(\mathbf{r};\,\mathbf{r}')\right]. \quad \text{(A22)}$$

so that the horizontal velocity at any point in the model atmosphere is determined by the instantaneous positions of the contours alone. This expression forms the basis of the nonlinear contour dynamics simulations.

Since the potential vorticity is assumed to be piecewise uniform in each active layer, the structure of the potential vorticity field is completely characterized by the contours separating the different regions of uniform potential vorticity. This situation suggests conversion of the area integrals over R_1^j in (A21) and (A22) into line integrals along the contours C^j. This conversion can be achieved by expressing both $\tilde{G}^k$ and $\nabla\tilde{G}^k$ in terms of divergences (see Verkley 1994), that is,

$$\tilde{G}^k(\mathbf{r};\,\mathbf{r}') = \frac{1}{\tilde{F}^k}\left[\nabla'^2 \tilde{V}^k(\mathbf{r};\,\mathbf{r}') - \frac{1}{4\pi}\right], \quad \text{(A23)}$$

$$\nabla\tilde{G}^k(\mathbf{r};\,\mathbf{r}') = \nabla' \cdot [\tilde{G}^k(\mathbf{r};\,\mathbf{r}')\mathbf{T}(\mathbf{r};\,\mathbf{r}')], \quad \text{(A24)}$$

where $\tilde{V}^k$ is a scalar function defined by

$$\tilde{V}^k(\mathbf{r};\,\mathbf{r}') = \tilde{G}^k(\mathbf{r};\,\mathbf{r}') - \tilde{H}(\mathbf{r};\,\mathbf{r}'), \quad \text{(A25)}$$

with

$$\tilde{H}(\mathbf{r};\,\mathbf{r}') = \frac{1}{4\pi}\ln\sin^2\left(\frac{\theta''}{2}\right), \quad \text{(A26)}$$

and $\mathbf{T}$ is a tensor, defined by

$$\begin{aligned}\mathbf{T}(\mathbf{r};\,\mathbf{r}') \equiv\; & -\frac{\cos\phi'}{\cos\phi}\mathbf{i}'\mathbf{i} + \sin\phi'\sin(\lambda - \lambda')\mathbf{i}'\mathbf{j} \\ & - \cos(\lambda - \lambda')\mathbf{j}'\mathbf{j}. \quad \text{(A27)}\end{aligned}$$

Substitution of (A23) into (A21) and use of Gauss's theorem give

$$\psi^i(\mathbf{r}) = \sum_{jk} \chi^{ik}\tilde{\chi}^{kj}\left[-\frac{q_0^j}{\tilde{F}^k} + \frac{f(\mathbf{r})}{\tilde{F}^k + 2} - \frac{\Delta q^j}{\tilde{F}^k}\frac{A_1^j}{4\pi} + \frac{\Delta q^j}{\tilde{F}^k}\oint_{C^j} dl'\mathbf{n}' \cdot \nabla'\tilde{V}^k(\mathbf{r};\,\mathbf{r}')\right], \quad \text{(A28)}$$

where A_1^j is the area of R_1^j, dl' is a line element along the contour C^j, and $\mathbf{n}'$ is a unit vector locally perpendicular to the contour and to $\mathbf{k}$ and pointing away from R_1^j. Substitution of (A24) into (A22) and use of Gauss's theorem again give

$$\nabla\psi^i(\mathbf{r}) = \sum_{jk} \chi^{ik}\tilde{\chi}^{kj}\left\{\frac{\nabla f(\mathbf{r})}{\tilde{F}^k + 2} + \Delta q^j \oint_{C^j} dl'[\mathbf{n}' \cdot \mathbf{T}(\mathbf{r};\,\mathbf{r}')]\tilde{G}^k(\mathbf{r};\,\mathbf{r}')\right\}, \quad \text{(A29)}$$

c. Zonal flow

For a zonal flow, the streamfunction (A18) is given by, substituting 2 $\sin\phi$ for $f(\mathbf{r})$,

$$\Psi^i(\phi) = \sum_{jk} \chi^{ik}\tilde{\chi}^{kj}\left[-\frac{q_0^j}{\tilde{F}^k} + \frac{2\sin\phi}{\tilde{F}^k + 2} + \Delta q^j \xi^{jk}(\phi)\right], \tag{A30}$$

where the symbol Ψ is used to indicate the zonal streamfunction. Here, the field ξ^{jk} is a function of ϕ only and is the solution of (A19), which in the zonal case reads

$$\nabla^2 \xi^{jk}(\phi) - \tilde{F}^k \xi^{jk}(\phi) = \mathcal{H}^j(\phi), \tag{A31}$$

with $\mathcal{H}^j(\phi)$ defined by

$$\mathcal{H}^j(\phi) = \begin{cases} 1, & \phi > \phi_C^j \\ 0, & \phi < \phi_C^j. \end{cases} \tag{A32}$$

The solution ξ^{jk} can be written as

$$\xi^{jk}(\phi) = \begin{cases} \xi_1^{jk}(\phi), & \phi > \phi_C^j \\ \xi_0^{jk}(\phi), & \phi < \phi_C^j, \end{cases} \tag{A33}$$

where

$$\xi_1^{jk}(\phi) = -\frac{1}{\tilde{F}^k} + B_1^{jk} P^0_{-1/2+i\gamma^k}(\sin\phi), \tag{A34a}$$

$$\xi_0^{jk}(\phi) = B_0^{jk} P^0_{-1/2+i\gamma^k}(-\sin\phi). \tag{A34b}$$

The fact that (A33)–(A34) is indeed a regular solution of (A31) is a consequence of the fact that products of the Legendre functions $P^m_{-1/2+i\gamma^k}(x)$, where $x = \pm \sin\phi$, and either $\cos(m\lambda)$ or $\sin(m\lambda)$ are eigenfunctions of the Laplace operator with real and positive eigenvalues $\frac{1}{4} + (\gamma^k)^2$ and therefore are solutions of the homogeneous Helmholtz equation if γ^k is chosen such that $\tilde{F}^k = \frac{1}{4} + (\gamma^k)^2$. The functions $P^m_{-1/2+i\gamma^k}(x)$ decrease monotonically from positive infinity at $x = -1$ to either 0 (if $m \neq 0$) or 1 (if $m = 0$) at $x = 1$. A few graphs of the functions $P^m_{-1/2+i\gamma}(x)$ and an algorithm to calculate them can be found in Verkley (1984). Continuity of ξ^{jk} and its first derivative with respect to ϕ at $\phi = \phi_C^j$ leads to the following expressions for the constants B_0^{jk} and B_1^{jk}:

$$B_0^{jk} = -\frac{1}{D(\gamma^k, \phi_C^j, 1)}\,[P^1_{-1/2+i\gamma^k}(-\sin\phi_C^j)]^{-1}, \tag{A35a}$$

$$B_1^{jk} = \frac{1}{D(\gamma^k, \phi_C^j, 1)}[P^1_{-1/2+i\gamma^k}(\sin\phi_C^j)]^{-1}, \tag{A35b}$$

where the function $D(\gamma, \phi, m)$, with $m = 0, 1, 2, \ldots$, is defined as

$$D(\gamma, \phi, m) \equiv \frac{P^{m+1}_{-1/2+i\gamma}(-\sin\phi)}{P^m_{-1/2+i\gamma}(-\sin\phi)} + \frac{P^{m+1}_{-1/2+i\gamma}(\sin\phi)}{P^m_{-1/2+i\gamma}(\sin\phi)}, \tag{A36}$$

and use was made of certain recurrency relations in the same way as in Verkley (1994). Note that the function $D(\gamma, \phi, m)$ is positive since the Legendre functions $P^m_{-1/2+i\gamma}(x)$ are also positive. It can be shown that (A33) and (A34) are consistent with the more general expression (A20) when this expression is applied to zonal contours. The zonal velocity field U^i follows from (1).

d. Perturbed flow

For a general perturbation of the contour C^j, it follows from (A18) and (A20) that we have for the perturbation in the streamfunction, denoted by $\delta\psi^i(\mathbf{r})$,

$$\delta\psi^i(\mathbf{r}) = \sum_{jk} \chi^{ik}\tilde{\chi}^{kj}\Delta q^j \delta\xi^{jk}(\mathbf{r}), \tag{A37}$$

where $\delta\xi^{jk}(\mathbf{r})$ is given by

$$\delta\xi^{jk}(\mathbf{r}) = \int_{\delta R_1^j} dS'\tilde{G}^k(\mathbf{r}; \mathbf{r}'), \tag{A38}$$

in which expression δR_1^j denotes the perturbation of the region R_1^j. For an infinitesimal perturbed contour, of which the perturbation can be described by a function $\delta n'(l')$, where l' is the arclength along the contour and $\delta n'$ is an infinitesimal distance in the direction of the outward normal of the contour, we can write

$$\delta\xi^{jk}(\mathbf{r}) = \oint_{C^j} dl'\,\delta n'(l')\tilde{G}^k(\mathbf{r}; \mathbf{r}'). \tag{A39}$$

The expression above can also be written as

$$\delta\xi^{jk}(\mathbf{r}) = \int_S dS''\tilde{G}^k(\mathbf{r}; \mathbf{r}'')\delta\mathcal{H}^j(\mathbf{r}''), \tag{A40}$$

where $\delta\mathcal{H}^j(\mathbf{r})$ is given by

$$\delta\mathcal{H}^j(\mathbf{r}) = \oint_{C^j} dl'\,\delta n'(l')\delta(\mathbf{r}; \mathbf{r}'). \tag{A41}$$

Note that $\delta\mathcal{H}^j(\mathbf{r})$ is zero everywhere except on the contour C^j, where it has a delta-function structure with strength $\delta n'(l')$. From expression (A40), we infer that $\delta\xi^{jk}(\mathbf{r})$ is the solution of

$$\nabla^2\delta\xi^{jk}(\mathbf{r}) - \tilde{F}^k\delta\xi^{jk}(\mathbf{r}) = \delta\mathcal{H}^j(\mathbf{r}). \tag{A42}$$

By integrating this equation over a small region enclosing a small part of the contour C^j, we may verify that the projection of the gradient $\nabla\delta\xi^{jk}$ onto the outward normal $\mathbf{n}$ of C^j, going from just inside to just outside the contour, makes a jump of magnitude $\delta n'(l')$. Together with the requirement that $\delta\xi^{jk}$ be continuous at the contour and the fact that $\delta\mathcal{H}^j(\mathbf{r})$ is zero outside the contour, this gives us all we need to find $\delta\xi^{jk}$ for sinusoidal perturbations of zonal contours.

Let us go back to the zonal flows (11) and consider infinitesimal wavelike perturbations of these contours described by (12)–(13). Note that for zonal contours of this form, $\lambda\cos\phi_C^j$ fulfills the role of the arclength l,

and $-\delta\phi_C^i$ fulfills the role of δn. For $\delta\mathcal{H}^j(\mathbf{r})$ we therefore have, applying (A41),

$$\begin{aligned}\delta\mathcal{H}^j(\lambda, \phi, t) &= -\int_0^{2\pi} d\lambda' \cos\phi_C^j \mathrm{Re}[\epsilon^j \exp im(\lambda' - \omega t)] \\ &\quad \times \delta(\lambda, \phi; \lambda', \phi_C^j) \\ &= \delta(\phi - \phi_C^j)\mathrm{Re}[\epsilon^j \exp im(\lambda - \omega t)]. \end{aligned} \tag{A43}$$

We will search a solution of (A42) of the form

$$\delta\xi^{jk}(\lambda, \phi, t) = \nu^{jk}(\phi)\mathrm{Re}[\epsilon^j \exp im(\lambda - \omega t)], \tag{A44}$$

with

$$\nu^{jk}(\phi) = \begin{cases} \nu_1^{jk}(\phi), & \phi > \phi_C^j \\ \nu_0^{jk}(\phi), & \phi < \phi_C^j, \end{cases} \tag{A45}$$

$$\nu_1^{jk}(\phi) = b_1^{jk} P^m_{-1/2+i\gamma^k}(\sin\phi), \quad \text{and} \tag{A46a}$$

$$\nu_0^{jk}(\phi) = b_0^{jk} P^m_{-1/2+i\gamma^k}(-\sin\phi). \tag{A46b}$$

It follows from the properties of the Legendre functions that this solution satisfies (A42) both inside and outside the contour. The continuity of $\delta\xi^{jk}$ and the jump condition on the gradient $\delta\xi^{jk}$ lead to (as in Verkley 1994)

$$b_1^{jk} = \frac{1}{D(\gamma^k, \phi_C^j, m)}[P^m_{-1/2+i\gamma^k}(\sin\phi_C^j)]^{-1}, \tag{A47a}$$

$$b_0^{jk} = \frac{1}{D(\gamma^k, \phi_C^j, m)}[P^m_{-1/2+i\gamma^k}(-\sin\phi_C^j)]^{-1}, \tag{A47b}$$

where $D(\gamma, \phi, m)$ is the function defined in (A36). The perturbation streamfunction, as given by (A37), can then be written as

$$\delta\psi^i(\lambda, \phi, t) = \sum_{jk} \chi^{ik}\tilde{\chi}^{kj}\Delta q^j \nu^{jk}(\phi)\mathrm{Re}[\epsilon^j \exp im(\lambda - \omega t)] \tag{A48}$$

or

$$\delta\psi^i(\lambda, \phi, t) = \sum_j Z^{ij}(\phi)\mathrm{Re}[\epsilon^j \exp im(\lambda - \omega t)], \tag{A49}$$

where the fields $Z^{ij}(\phi)$ are defined by

$$Z^{ij}(\phi) = \sum_k \chi^{ik}\tilde{\chi}^{kj}\Delta q^j \nu^{jk}(\phi). \tag{A50}$$

REFERENCES

Baehr, C., B. Pouponneau, F. Ayrault, and A. Joly, 1999: Dynamical characterization of the FASTEX cyclogenesis cases. *Quart. J. Roy. Meteor. Soc.,* **125,** 3469–3494.

Bjerknes, J., 1919: On the structure of moving cyclones. *Geofys. Publ.,* **1,** 1–8.

——, and H. Solberg, 1921: Meteorological conditions for the formation of rain. *Geofys. Publ.,* **2,** 1–60.

——, and ——, 1922: Life cycle of cyclones and the polar front theory of atmospheric circulation. *Geofys. Publ.,* **3,** 1–18.

Bretherton, F. P., 1966a: Critical layer instability in baroclinic flows. *Quart. J. Roy. Meteor. Soc.,* **92,** 325–334.

——, 1966b: Baroclinic instability and the short wavelength cut-off in terms of potential vorticity. *Quart. J. Roy. Meteor. Soc.,* **92,** 335–345.

Charney, J. G., 1947: The dynamics of long waves in a baroclinic westerly current. *J. Meteor.,* **4,** 135–163.

——, and M. E. Stern, 1962: On the stability of internal baroclinic jets in a rotating atmosphere. *J. Atmos. Sci.,* **19,** 159–172.

Cressman, G. P., 1958: Barotropic divergence and very long atmospheric waves. *Mon. Wea. Rev.,* **86,** 293–297.

Daley, R., 1983: Linear non-divergent mass-wind laws on the sphere. *Tellus,* **35A,** 17–27.

Dritschel, D. G., 1989: Contour dynamics and contour surgery: Numerical algorithms for extended, high-resolution modelling of vortex dynamics in two-dimensional, inviscid, incompressible flows. *Comput. Phys. Rep.,* **10,** 77–146.

——, and M. H. P. Ambaum, 1997: A contour-advective semi-Lagrangian numerical algorithm for simulating fine-scale conservative dynamical fields. *Quart. J. Roy. Meteor. Soc.,* **123,** 1097–1130.

Eady, E. T., 1949: Long waves and cyclone waves. *Tellus,* **1,** 33–52.

Haynes, P., J. Scinocca, and M. Greenslade, 2001: Formation and maintenance of the extratropical tropopause by baroclinic eddies. *Geophys. Res. Lett.,* **28,** 4179–4182.

Hoskins, B. J., M. E. McIntyre, and A. W. Robertson, 1985: On the use and significance of isentropic potential vorticity maps. *Quart. J. Roy. Meteor. Soc.,* **111,** 877–946.

Palmén, E., and C. W. Newton, 1969: *Atmospheric Circulation Systems.* Academic Press, 603 pp.

Pedlosky, J., 1987: *Geophysical Fluid Dynamics.* Springer-Verlag, 710 pp.

Phillips, N. A., 1951: A simple three-dimensional model for the study of large-scale extratropical flow patterns. *J. Meteor.,* **8,** 381–394.

——, 1954: Energy transformations and meridional circulations associated with simple baroclinic waves in a two-level, quasi-geostrophic model. *Tellus,* **6,** 273–286.

Reed, R. J., 1955: A study of a characteristic type of upper-level frontogenesis. *J. Meteor.,* **12,** 226–237.

Scheele, M. P., P. C. Siegmund, and P. F. J. van Velthoven, 1996: Sensitivity of trajectories to data resolution and its dependence on the starting point: In or outside a tropopause fold. *Meteor. Appl.,* **3,** 267–273.

Thorncroft, C. D., B. J. Hoskins, and M. E. McIntyre, 1993: Two paradigms of baroclinic-wave life-cycle behaviour. *Quart. J. Roy. Meteor. Soc.,* **119,** 17–55.

Verkley, W. T. M., 1984: The construction of barotropic modons on a sphere. *J. Atmos. Sci.,* **41,** 2492–2504.

——, 1994: Tropopause dynamics and planetary waves. *J. Atmos. Sci.,* **51,** 509–529.

——, 2000: On the vertical velocity in an isentropic layer. *Quart. J. Roy. Meteor. Soc.,* **126,** 263–274.

——, 2001: Salmon's Hamiltonian approach to balanced flow applied to a one-layer isentropic model of the atmosphere. *Quart. J. Roy. Meteor. Soc.,* **127,** 579–600.

Wilkinson, J. H., 1965: *The Algebraic Eigenvalue Problem.* Oxford University Press, 662 pp.